Measurement of $B^+ \to \tau^+ \nu_{\tau}$ branching fraction with a hadronic tagging method at Belle II

```
I. Adachi, K. Adamczyk, H. Ahmed, Y. Ahn, H. Aihara, N. Akopov, M. Alhakami, A. Aloisio, N. Althubiti,
    M. Angelsmark, N. Anh Ky, D. M. Asner, H. Atmacan, V. Aushev, M. Aversano, R. Ayad, V. Babu,
     N. K. Baghel<sup>®</sup>, S. Bahinipati<sup>®</sup>, P. Bambade<sup>®</sup>, Sw. Banerjee<sup>®</sup>, M. Bartl<sup>®</sup>, J. Baudot<sup>®</sup>, A. Baur<sup>®</sup>, A. Beaubien<sup>®</sup>,
F. Becherer<sup>®</sup>, J. Becker<sup>®</sup>, J. V. Bennett<sup>®</sup>, F. U. Bernlochner<sup>®</sup>, V. Bertacchi<sup>®</sup>, E. Bertholet<sup>®</sup>, M. Bessner<sup>®</sup>, S. Bettarini<sup>®</sup>,
B. Bhuyan, F. Bianchi, D. Biswas, A. Bobrov, D. Bodrov, A. Bondar, J. Borah, A. Boschetti, A. Bozek, A. Bozek,
M. Bračko<sup>®</sup>, P. Branchini<sup>®</sup>, R. A. Briere<sup>®</sup>, T. E. Browder<sup>®</sup>, A. Budano<sup>®</sup>, S. Bussino<sup>®</sup>, Q. Campagna<sup>®</sup>, M. Campajola<sup>®</sup>,
  L. Cao, G. Casarosa, C. Cecchi, M.-C. Chang, P. Cheema, B. G. Cheon, K. Chilikin, K. Chirapatpimol,
          H.-E. Cho, K. Cho, S.-J. Cho, S.-K. Cho, S. Choudhury, J. Cochran, L. Corona, J. X. Cui,
E. De La Cruz-Burelo, S. A. De La Motte, G. De Nardo, G. De Pietro, R. de Sangro, M. Destefanis, S. Dey,
A. Di Canto, J. Dingfelder, Z. Doležal, T. V. Dong, M. Dorigo, K. Dugic, G. Dujany, P. Ecker, D. Epifanov,
J. Eppelt<sup>®</sup>, T. Ferber<sup>®</sup>, T. Fillinger<sup>®</sup>, C. Finck<sup>®</sup>, G. Finocchiaro<sup>®</sup>, A. Fodor<sup>®</sup>, F. Forti<sup>®</sup>, B. G. Fulsom<sup>®</sup>, A. Gabrielli<sup>®</sup>,
  A. Gale<sup>®</sup>, M. Garcia-Hernandez<sup>®</sup>, L. Gärtner<sup>®</sup>, G. Gaudino<sup>®</sup>, V. Gaur<sup>®</sup>, A. Gaz<sup>®</sup>, A. Gellrich<sup>®</sup>, G. Ghevondyan<sup>®</sup>,
D. Ghosh, H. Ghumaryan, G. Giakoustidis, R. Giordano, A. Giri, P. Gironella Gironell, B. Gobbo, R. Godang,
  O. Gogota<sup>®</sup>, P. Goldenzweig<sup>®</sup>, W. Gradl<sup>®</sup>, E. Graziani<sup>®</sup>, D. Greenwald<sup>®</sup>, Z. Gruberová<sup>®</sup>, Y. Guan<sup>®</sup>, K. Gudkova<sup>®</sup>,
   I. Haide<sup>®</sup>, H. Hayashii<sup>®</sup>, S. Hazra<sup>®</sup>, C. Hearty<sup>®</sup>, I. Heredia de la Cruz<sup>®</sup>, T. Higuchi<sup>®</sup>, M. Hoek<sup>®</sup>, M. Hohmann<sup>®</sup>,
R. Hoppe<sup>®</sup>, P. Horak<sup>®</sup>, C.-L. Hsu<sup>®</sup>, A. Huang<sup>®</sup>, T. Iijima<sup>®</sup>, N. Ipsita<sup>®</sup>, A. Ishikawa<sup>®</sup>, R. Itoh<sup>®</sup>, M. Iwasaki<sup>®</sup>, P. Jackson<sup>®</sup>,
D. Jacobi<sup>®</sup>, W. W. Jacobs<sup>®</sup>, D. E. Jaffe<sup>®</sup>, E.-J. Jang<sup>®</sup>, Y. Jin<sup>®</sup>, A. Johnson<sup>®</sup>, K. K. Joo<sup>®</sup>, H. Junkerkalefeld<sup>®</sup>, J. Kandra<sup>®</sup>,
K. H. Kang, G. Karyan, T. Kawasaki, C. Ketter, C. Kiesling, D. Y. Kim, J.-Y. Kim, K.-H. Kim, H. Kindo,
        K. Kinoshita<sup>®</sup>, P. Kodyš<sup>®</sup>, T. Koga<sup>®</sup>, S. Kohani<sup>®</sup>, K. Kojima<sup>®</sup>, A. Korobov<sup>®</sup>, S. Korpar<sup>®</sup>, E. Kovalenko<sup>®</sup>,
R. Kowalewski, P. Križan, P. Krokovny, T. Kuhr, D. Kumar, R. Kumar, K. Kumar, T. Kunigo, A. Kuzmin,
Y.-J. Kwon, T. Lam, J. S. Lange, T. S. Lau, M. Laurenza, R. Leboucher, F. R. Le Diberder, M. J. Lee, P. Leo,
L. K. Li<sup>®</sup>, W. Z. Li<sup>®</sup>, Y. Li<sup>®</sup>, J. Libby<sup>®</sup>, S. Lin<sup>®</sup>, M. H. Liu<sup>®</sup>, Q. Y. Liu<sup>®</sup>, Z. Q. Liu<sup>®</sup>, D. Liventsev<sup>®</sup>, S. Longo<sup>®</sup>, T. Lueck<sup>®</sup>,
C. Lyu, Y. Ma, C. Madaan, M. Maggiora, R. Maiti, G. Mancinelli, R. Manfredi, E. Manoni, M. Mantovano,
D. Marcantonio, S. Marcello, C. Marinas, C. Martellini, A. Martens, T. Martinov, L. Massacces, M. Masuda,
 K. Matsuoka<sup>®</sup>, S. K. Maurya<sup>®</sup>, M. Maushart<sup>®</sup>, J. A. McKenna<sup>®</sup>, F. Meier<sup>®</sup>, D. Meleshko<sup>®</sup>, M. Merola<sup>®</sup>, C. Miller<sup>®</sup>,
    M. Mirra, K. Miyabayashi, R. Mizuk, S. Mondal, S. Moneta, H.-G. Moser, I. Nakamura, M. Nakao,
H. Nakazawa<sup>®</sup>, Z. Natkaniec<sup>®</sup>, A. Natochii<sup>®</sup>, M. Nayak<sup>®</sup>, M. Neu<sup>®</sup>, M. Niiyama<sup>®</sup>, S. Nishida<sup>®</sup>, S. Ogawa<sup>®</sup>, R. Okubo<sup>®</sup>,
H. Ono<sup>®</sup>, G. Pakhlova<sup>®</sup>, S. Pardi<sup>®</sup>, J. Park<sup>®</sup>, K. Park<sup>®</sup>, S.-H. Park<sup>®</sup>, B. Paschen<sup>®</sup>, S. Patra<sup>®</sup>, S. Paul<sup>®</sup>, T. K. Pedlar<sup>®</sup>,
I. Peruzzi<sup>®</sup>, R. Peschke<sup>®</sup>, L. E. Piilonen<sup>®</sup>, T. Podobnik<sup>®</sup>, S. Pokharel<sup>®</sup>, C. Praz<sup>®</sup>, S. Prell<sup>®</sup>, E. Prencipe<sup>®</sup>, M. T. Prim<sup>®</sup>,
S. Privalovo, I. Prudijevo, H. Purwaro, S. Raizo, K. Ravindrano, J. U. Rehmano, M. Reifo, S. Reitero, M. Remnevo,
   D. Ricalde Herrmann<sup>®</sup>, I. Ripp-Baudot<sup>®</sup>, G. Rizzo<sup>®</sup>, S. H. Robertson<sup>®</sup>, J. M. Roney<sup>®</sup>, A. Rostomyan<sup>®</sup>, N. Rout<sup>®</sup>,
    D. A. Sanders, S. Sandilya, L. Santelj, V. Savino, B. Scavino, C. Schmitt, J. Schmitt, S. Schneider,
C. Schwanda, Y. Seino, K. Senyo, M. E. Sevior, C. Sfienti, W. Shan, X. D. Shi, T. Shillington, J.-G. Shiu,
D. Shtol<sup>®</sup>, A. Sibidanov<sup>®</sup>, F. Simon<sup>®</sup>, J. B. Singh<sup>®</sup>, J. Skorupa<sup>®</sup>, R. J. Sobie<sup>®</sup>, M. Sobotzik<sup>®</sup>, A. Soffer<sup>®</sup>, A. Sokolov<sup>®</sup>,
E. Solovieva, S. Spataro, B. Spruck, M. Starič, S. Stefkova, R. Stroili, Y. Sue, M. Sumihama, M. Takizawa,
    F. Tenchini, A. Thaller, O. Tittel, R. Tiwary, E. Torassa, K. Trabels, I. Tsaklidis, I. Ueda, T. Uglov,
K. Unger<sup>®</sup>, K. Uno<sup>®</sup>, S. Uno<sup>®</sup>, P. Urquijo<sup>®</sup>, Y. Ushiroda<sup>®</sup>, S. E. Vahsen<sup>®</sup>, R. van Tonder<sup>®</sup>, K. E. Varvell<sup>®</sup>, M. Veronesi<sup>®</sup>,
A. Vinokurova<sup>®</sup>, V. S. Vismaya<sup>®</sup>, V. Vobbilisetti<sup>®</sup>, R. Volpe<sup>®</sup>, S. Wallner<sup>®</sup>, M.-Z. Wang<sup>®</sup>, A. Warburton<sup>®</sup>, S. Watanuki<sup>®</sup>,
     C. Wessel, E. Won, X. P. Xu, B. D. Yabsley, S. Yamada, W. Yan, S. B. Yang, J. Yelton, J. H. Yin,
K. Yoshihara, C. Z. Yuan, J. Yuan, L. Zani, F. Zeng, B. Zhang, V. Zhilich, Q. D. Zhou, L. Zhu, and R. Žlebčík
```

(Belle II Collaboration)

(Received 7 February 2025; accepted 10 September 2025; published 3 October 2025)

Published by the American Physical Society under the terms of the Creative Commons Attribution 4.0 International license. Further distribution of this work must maintain attribution to the author(s) and the published article's title, journal citation, and DOI. Funded by SCOAP³.

We present a measurement of the branching fraction of $B^+ \to \tau^+ \nu_\tau$ decays using $387 \pm 6 \times 10^6 \ \Upsilon(4S)$ collected between 2019 and 2022 with the Belle II detector at the SuperKEKB e^+e^- collider. We reconstruct the accompanying B^- meson using the hadronic tagging method, while $B^+ \to \tau^+ \nu_\tau$ candidates are identified in the recoil. We find evidence for $B^+ \to \tau^+ \nu_\tau$ decays at 3.0 standard deviations, including systematic uncertainties. The measured branching fraction is $\mathcal{B}(B^+ \to \tau^+ \nu_\tau) = [1.24 \pm 0.41 (\mathrm{stat}) \pm 0.19 (\mathrm{syst})] \times 10^{-4}$.

DOI: 10.1103/dcwd-5tg4

I. INTRODUCTION

The leptonic decay $B^+ \to \tau^+ \nu_\tau$ [1] is a process with a clean theoretical prediction in the standard model (SM) and is potentially sensitive to contributions from beyond-the-standard-model (BSM) physics. In the SM, the branching fraction is given by

$$\mathcal{B}(B^+ \to \tau^+ \nu_\tau) = \frac{G_F^2 m_B m_\tau^2}{8\pi} \left[1 - \frac{m_\tau^2}{m_B^2} \right]^2 f_B^2 |V_{ub}|^2 \tau_B, \qquad (1)$$

where G_F is the Fermi coupling constant, m_B and m_τ are the masses of the charged B^+ meson and the τ lepton, respectively, f_B is the B^+ meson decay constant, V_{ub} is the Cabibbo-Kobayashi-Maskawa (CKM) matrix element related to u and b quarks, and τ_B the lifetime of the B^+ meson. All of the quantities in Eq. (1) are measured experimentally [2] except for f_B , which is determined from lattice quantum chromodynamics (LQCD) simulations [3].

Assuming the SM and the precise calculation of f_B from LQCD, the $B^+ \to \tau^+ \nu_\tau$ decay mode provides a direct measurement of the CKM matrix element $|V_{ub}|$ that is independent of exclusive and inclusive semileptonic $B \to X_u \ell \nu_\ell$ decays, which are typically studied for this purpose [4]. Moreover, in leptonic decays, the theoretical uncertainty will not be a limiting factor soon; the FLAG working group estimates an uncertainty below 1% [3]. The $B^+ \to \tau^+ \nu_\tau$ decay is sensitive to BSM contributions, such as those predicted by models like the two Higgs doublet model [5–7], or various supersymmetric extensions of the SM [8,9]. In these models the branching fraction of the $B^+ \to \tau^+ \nu_\tau$ decay can be enhanced (or suppressed) by a factor up to 4 [10], taking into account experimental constraints from previous measurements. Therefore, a precise measurement

TABLE I. Published results for $\mathcal{B}(B^+ \to \tau^+ \nu_{\tau})$ by Belle, *BABAR*, and the PDG average.

Experiment	Tag	$\mathcal{B}(10^{-4})$
Belle [12]	Hadronic	$0.72^{+0.27}_{-0.25} \pm 0.11$
BABAR [11]	Hadronic	$1.83^{+0.53}_{-0.49} \pm 0.24$
Belle [13]	Semileptonic	$1.25 \pm 0.28 \pm 0.27$
<i>BABAR</i> [14]	Semileptonic	$1.7 \pm 0.8 \pm 0.2$
PDG [2]		1.09 ± 0.24

of the branching fraction can also be used to constrain the parameter space of these models.

Belle and *BABAR* measured $\mathcal{B}(B^+ \to \tau^+ \nu_\tau)$ reconstructing the accompanying B^- meson in hadronic decays [11,12] or semileptonic decays [13,14]. Table I shows past measurements and the current world average.

The measurement described in this paper is based on data collected by the Belle II experiment at the SuperKEKB electron-positron collider between 2019 and 2022 and has an integrated luminosity of 365.4 ± 1.7 fb⁻¹ [15], corresponding to a number of produced $\Upsilon(4S)$ estimated to be $n_{\Upsilon(4S)} = (387 \pm 6) \times 10^6$. In addition, we use 42.3 fb⁻¹ of data collected at the slightly lower center-of-mass energy of 10.52 GeV (off resonance) to calibrate the background from continuum $e^+e^- \rightarrow q\bar{q}$ (where q=u, d, s, c) and $e^+e^- \rightarrow \tau^+\tau^-$ events in a data-driven way. A B^- meson is fully reconstructed in an exclusive hadronic decay (B_{tag}) and the remaining charged-particle trajectories (tracks) and neutral energy deposits in the calorimeter (clusters) are examined for the signature of a $B^+ \to \tau^+ \nu_{\tau}$ decay $(B_{\rm sig})$. We consider four τ^+ decays with a single charged particle in the final state: $\tau^+ \to e^+ \ \nu_e \ \bar{\nu}_\tau, \ \tau^+ \to \mu^+ \ \nu_\mu \ \bar{\nu}_\tau, \ \tau^+ \to \pi^+$ $\bar{\nu}_{\tau}$, and $\tau^{+} \rightarrow \rho^{+} \bar{\nu}_{\tau}$ channels, where ρ is the $\rho(770)$. These modes account for approximately 72% of all τ decays [2]. Each mode is treated as a distinct signal category. We define a set of selection requirements to suppress the backgrounds for which either the B_{tag} or the B_{sig} are misidentified. We optimize the signal selection on simulation, which is corrected and validated on several control samples. We extract the branching fraction using a simultaneous two-dimensional maximum likelihood fit to two discriminating variables, the residual energy in the electromagnetic calorimeter not associated with the reconstructed B^+B^- pair, and the missing mass squared of the event.

II. BELLE II DETECTOR AND SIMULATION

The Belle II experiment [16] is located at the SuperKEKB accelerator [17], which collides 7 GeV electrons and 4 GeV positrons at and near the $\Upsilon(4S)$ resonance. The Belle II detector [16] has a cylindrical geometry arranged around the interaction point (IP), which is enclosed by a beryllium beam pipe with an inner radius of 1 cm, and includes a two-layer silicon-pixel detector (PXD) surrounded by a four-layer double-sided siliconstrip detector (SVD) [18] and a 56-layer central drift

chamber (CDC). These detectors reconstruct tracks of charged particles. In this work, we analyze the data for the period when only one-sixth of the second layer of the PXD was installed. Surrounding the CDC, which also provides ionization-energy-loss measurements, is a timeof-propagation counter (TOP) [19] in the central region and an aerogel-based ring-imaging Cherenkov counter (ARICH) in the forward end cap region. These detectors provide charged-particle identification (PID). Surrounding the TOP and ARICH is an electromagnetic calorimeter (ECL) based on CsI(Tl) crystals that primarily provide energy and timing measurements for photons and electrons. Outside of the ECL is a superconducting solenoid magnet, which provides an axial magnetic field of 1.5 T. A K_L^0 and muon identification system is located outside of the magnet and consists of flux-return iron plates interspersed with resistive plate chambers and plastic scintillators. The central axis of the solenoid defines the z axis of the laboratory frame, pointing approximately in the direction of the electron beam.

We use Monte Carlo (MC) simulated events to optimize selection criteria, calculate reconstruction efficiencies, and study sources of background. The $B\bar{B}$ samples are generated with EvtGen [20]. Continuum $e^+e^- \to q\bar{q}$ (q=u,d,s,c) and $e^+e^- \to \tau^+\tau^-$ events are generated with KKMC [21]. The fragmentation of $q\bar{q}$ uses PYTHIA8 [22], and τ decays are simulated by TAUOLA [23]. Final-state radiation is simulated by PHOTOS [24,25]. Geant4 [26] is used to simulate the detector response to the passage of particles. For the simulated signal, we produce 4×10^7 events, in which one B meson decays exclusively to the $B^+ \to \tau^+\nu_\tau$ final state, and the other B meson decays generically.

For the $B\bar{B}$, $q\bar{q}$, and $\tau^+\tau^-$ backgrounds we use simulated samples with equivalent integrated luminosities of 2.8, 1, and 0.6 ab⁻¹, respectively. Both experimental and simulated data are processed using the Belle II analysis software framework [27].

III. RECONSTRUCTION AND EVENT SELECTION

To consider an event for further analysis we require the reconstruction of three or more tracks, each with an impact parameter with respect to the IP of less than 2 cm along the z axis and 0.5 cm in the transverse direction; three or more ECL clusters with E > 100 MeV and within the CDC acceptance; a minimum transverse momentum of 100 MeV/c for each of the charged particles; and a total energy of reconstructed tracks and ECL clusters greater than 4 GeV.

Simulation samples and data are then passed through the full event interpretation (FEI) [28], a hierarchical multivariate algorithm that fully reconstructs the $B_{\rm tag}$ in thousands of possible decay chains. The output of the FEI algorithm for each event is a set of reconstructed $B_{\rm tag}$ candidates with an associated score ($\mathcal{O}_{\rm FEI}$); the higher the

 \mathcal{O}_{FEI} , the higher the expected purity of the candidate. We require $\mathcal{O}_{\text{FEI}} > 0.001$ and the resulting fraction of $\Upsilon(4S)$ events with a correctly reconstructed charged B_{tag} candidate is estimated from simulations to be approximately 0.30% with a purity of 29% [29]. The average B_{tag} candidate multiplicity in signal events is 1.02. We retain one B_{tag} candidate per event, choosing the candidate with the highest value of \mathcal{O}_{FEI} .

We use two kinematic variables to discriminate between events with a correctly reconstructed $B_{\rm tag}$ candidate and misreconstructed events: the beam-energy-constrained mass $M_{\rm bc} = \sqrt{(E_{\rm beam}^*)^2/c^4 - |\vec{p}_{\rm tag}^*|^2/c^2}$ and the energy difference $\Delta E = E_{\rm tag}^* - E_{\rm beam}^*$, where $\vec{p}_{\rm tag}^*$ ($E_{\rm tag}^*$) is the reconstructed momentum (energy) of the $B_{\rm tag}$ and $E_{\rm beam}^*$ is the beam energy, all evaluated in the center of mass (c.m.) frame. We require $M_{\rm bc} > 5.27~{\rm GeV}/c^2$ and $-0.15 < \Delta E < 0.1~{\rm GeV}$.

The $B_{\rm sig}$ is reconstructed from all the remaining tracks and neutral objects (ECL clusters with no tracks associated) not used to reconstruct the B_{tag} . We consider four different signal categories identifying the following final states: $\tau^+ \to e^+ \ \nu_e \ \bar{\nu}_{\tau}, \ \tau^+ \to \mu^+ \ \nu_{\mu} \ \bar{\nu}_{\tau}, \ \tau^+ \to \pi^+ \ \bar{\nu}_{\tau}, \ {\rm and} \ \tau^+ \to$ ρ^+ $\bar{\nu}_{\tau}$. For this purpose, in addition to the tracks associated with the B_{tag} , we require only one other track in the event, with a charge opposite to the B_{tag} charge and a momentum p > 0.5 GeV/c. The PID criteria to distinguish between electron, muon, and pion hypotheses are based on multivariate classifiers that utilize information from all subdetectors. This information is combined into a boosted decision tree for electrons or a likelihood function for muons and pions. The likelihoods for the pion or muon hypotheses combine PID information from all subdetectors except the SVD and the PXD. From simulation, we estimate that PID selection criteria identify electrons, muons, and pions with efficiencies of 99%, 82%, and 97%; and that, respectively, 1%, 5%, and 3% of the selected samples are incorrectly identified. The selection criteria are mutually exclusive: each charged candidate is exclusively identified as electron or muon or pion. A bremsstrahlung correction in the $\tau^+ \to e^+ \nu_e \bar{\nu}_\tau$ decay mode is applied: the four-momentum of the electron candidates is corrected by adding the four-momenta of photons with an energy below 1.0 GeV within a cone of 0.05 rad around the electronmomentum vector. From pairs of ECL clusters not used to reconstruct B_{tag} , we reconstruct $\pi^0 \to \gamma \gamma$ candidates. We require these candidates to have an invariant mass in the range $120 < m_{\gamma\gamma} < 145 \text{ MeV}/c^2$, which corresponds to approximately $\pm 1\sigma$ of the mass resolution. The π^0 candidates are combined with the π^+ candidate to form ρ^+ candidate. If the ρ^+ candidate has a reconstructed invariant mass within $625 < m_{\pi^{+}\pi^{0}} < 925 \text{ MeV}/c^{2}$, the B_{sig} is assigned to the $\tau^+ \to \rho^+ \bar{\nu}_{\tau}$ category. Otherwise, the event is assigned to the $\tau^+ \to \pi^+ \bar{\nu}_{\tau}$ category. If multiple ρ^+

candidates are reconstructed, we choose the one closest to the ρ^+ mass [2].

Any cluster in the ECL not associated with the B_{tag} nor with the B_{sig} is subjected to a procedure that rejects the clusters from beam-induced backgrounds, the interaction of hadronic particles with detector material (hadronic split-off showers), and neutral hadrons. The procedure uses two different multivariate classifiers, trained on a $B^0 \to D^{*-}$ ℓ^+ ν_ℓ data control sample as described in [30]. All the objects refined by this clean-up procedure represent the rest of the event (ROE).

The two most discriminating observables based on the ROE are the total residual energy from neutral clusters in the ECL ($E_{\rm ECL}^{\rm extra}$) and the square of missing four-momentum ($M_{\rm miss}^2$) calculated using the known beam energies and all the reconstructed objects,

$$p_{\text{miss}}^* = (2E_{\text{beam}}^*, 0, 0, 0) - p_{\text{tag}}^* - p_{\text{sig}}^* - p_{\text{ROE}}^*,$$
 (2)

where p_{tag}^* , p_{sig}^* , p_{ROE}^* are, respectively, the B_{tag} , the signal candidate, and the ROE objects four-momenta in the c.m. frame.

We suppress continuum $e^+e^- \rightarrow q\bar{q}$ and $e^+e^- \rightarrow \tau^+\tau^$ backgrounds by applying a loose selection on two eventshape variables. The first variable, $\cos \theta_{\rm T}$, is the cosine of the angle between the thrust axis of the B_{tag} and the thrust axis of its recoil. The thrust axis is defined as the unit vector \hat{t} that maximizes the thrust value $\sum |\hat{t} \cdot \vec{p}_i^*| / \sum |\vec{p}_i^*|$ where \vec{p}_i^* is the momentum of the *i*th final-state particle in the e^+e^- c.m. frame [31,32]. This variable discriminates between signal and background because $B\bar{B}$ events have an approximately uniform distribution, while continuum events consist of two back-to-back jets in the c.m. frame. The second variable is the ratio of Fox-Wolfram moments R_2 [33], which measures the degree of sphericity of the event with lower values for $B\bar{B}$ events and higher values for continuum events. We require $|\cos \theta_{\rm T}| < 0.9$ and $R_2 < 0.6$, selecting 73% of the signal and rejecting 66% of the $q\bar{q}$ and 99% of the $\tau^+\tau^-$ background events.

After these loose requirements, the remaining continuum events are still a significant fraction of the total background, especially for the hadronic modes $\tau^+ \to \pi^+ \ \bar{\nu}_{\tau}$ and $\tau^+ \to \rho^+ \ \bar{\nu}_{\tau}$, and need further suppression. Since there are no $B\bar{B}$ events in the off-resonance sample, we use it to estimate the

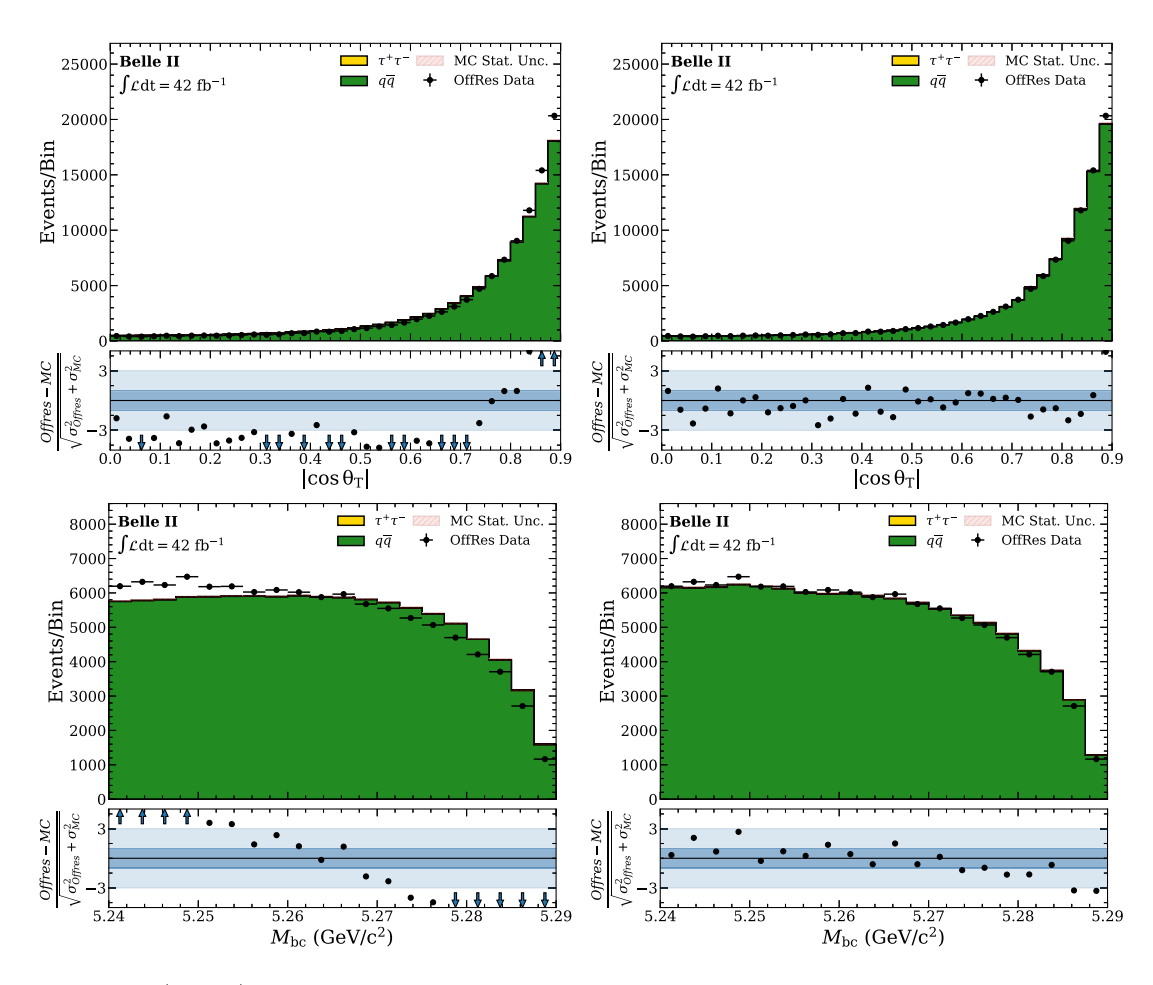


FIG. 1. Distributions of $|\cos \theta_{\rm T}|$ (top) and $M_{\rm bc}$ (bottom) in off-resonance data and continuum simulation before (left) and after (right) the continuum MC reweighting. The $\tau^+\tau^-$ component is negligible after the requirement on R_2 .

expected yield of the continuum background. Due to the lower statistics of the off-resonance sample after the signal selection procedure, we use simulation instead to describe the shapes of all variables for continuum events. Nevertheless, comparing simulation and off-resonance data we observe that continuum simulation does not adequately reproduce the shapes of many variables, as can be seen, for example, in Fig. 1 (left plots). We correct this mismodeling of the shapes by reweighting the simulation using the off-resonance data. We employ a fast boosted decision tree (FBDT) classifier [34] using the event-shape variables described in [35]. We use a simulated sample of continuum events and off-resonance data, which both correspond to 5×10^4 events, for training and validation. The weight w_{CR}^i for each event in simulation is defined as

$$w_{\rm CR}^i = \frac{\mathcal{O}_{\rm CR}^i}{1 - \mathcal{O}_{\rm CR}^i} \tag{3}$$

where $\mathcal{O}_{\text{CR}}^i$ is the output of the classifier for the event i [36,37]. Figure 1 shows the effect of the continuum reweighting on the simulated events for the $|\cos\theta_{\text{T}}|$ and M_{bc} distributions.

To further suppress continuum, simulated $B\bar{B}$ and reweighted continuum events are used to train another FBDT, based on event-shape variables described in [35]. The most discriminating variables are the super-Fox-Wolfram moments and the harmonic moments $B_l = \sum_i (p_i/\sqrt{s}) \times P_l(\cos \alpha_i)$, where P_l is the Legendre polynomial of order l, p_i is the momentum of the particle i, and α_i is the angle calculated with respect to the thrust axis of the B_{tag} recoil, as defined in [33]. As the leptonic and hadronic τ^+ channel inputs differ slightly, we train two independent FBDTs. To avoid bias, we use the classifier on simulated samples of continuum and simulated samples of $B\bar{B}$ of the same size (10⁵ events) for training and validation.

Finally, we exploit the following variables to further suppress backgrounds: \mathcal{O}_{FEI} , the output of the continuum suppression FBDT $\mathcal{O}_{\scriptscriptstyle{\text{CS}}}$, and the momentum of the reconstructed daughters of the τ^+ (e^+ , μ^+ , π^+ , and ρ^+) in the laboratory frame p_{cand} . More stringent requirements on \mathcal{O}_{FEI} improve the purity of the B_{tag} reconstruction; \mathcal{O}_{CS} is used for discrimination against continuum, especially necessary for hadronic τ^+ decay modes; a tight requirement on p_{cand} is effective to suppress $B\bar{B}$ background for hadronic modes produced in τ^+ two-body decays. We optimize the selection requirements independently for each channel to minimize the expected statistical uncertainty of signal yields. The signal yields are fitted (as explained in Sec. V) on pseudodatasets generated from signal and background simulations, assuming a signal branching fraction $\mathcal{B}(B^+ \to \tau^+ \nu_{\tau})_{PDG}$ and integrated luminosity as in data. Table II shows the optimized selection.

TABLE II. Optimized signal selection. ϵ is the efficiency for a $B^+ \to \tau^+ \nu_\tau$ event to be reconstructed in each signal category.

Signal category	$\mathcal{O}_{ ext{FEI}}$	$\mathcal{O}_{\scriptscriptstyle{ exttt{CS}}}$	$p_{\rm cand}~({\rm GeV}/c)$	ϵ (10 ⁻⁴)
e^+	> 0.01	< 0.8	> 0.5	7.3
$\mu^+ \ \pi^+$		< 0.6 < 0.6	> 1.4	7.6 3.4
$ ho^+$		< 0.0	> 1.4	3.4

IV. CALIBRATION AND MODEL VALIDATION

In this section, we discuss the efficiency correction for the signal and the $B\bar{B}$ simulations and $E_{\rm ECL}^{\rm extra}$ calibration and validation using several control samples and signal sidebands.

A. Efficiency correction

We determine the hadronic FEI reconstruction efficiency from simulation and then we correct it with a data-driven procedure using two data control samples. For the first one, we examine the recoil of the B_{tag} to select a sample of inclusive semileptonic decays $B^+ \to X \ell^+ \nu_\ell$, requiring the reconstruction of a high energy electron or muon. The details of the procedure are discussed elsewhere [29]. A second sample is selected requiring the presence of a hadronic decay $B^+ \to \bar{D}^{(*)0}$ π^+ , searching for the $\bar{D}^{(*)0}$ resonance in the π^+ recoil. The corrections to the B_{tag} reconstruction efficiency extracted from the hadronic sample are consistent with those from the semileptonic sample we use a combination of the correction factors from the two samples. The correction factors, obtained by comparing the yields in data and simulation, depend on the B_{tag} decay mode and vary between 0.6 and 1.1.

Additional corrections are applied to account for mismodeling in simulation of PID efficiencies and misidentification probabilities. They are evaluated by comparing data and simulation on pure samples of electrons and muons from an inclusive sample of $J/\psi \to \ell^+\ell^-$ decays and low multiplicity processes $e^+e^- \rightarrow \ell^+\ell^-$ (γ) and $e^+e^- \rightarrow e^+e^- \ell^+\ell^-$. To calibrate the charged pion identification we use a sample of pions from inclusive decays of $K_S^0 \to \pi^+\pi^-, D^{*+} \to D^0 \pi^+, \text{ and } \Lambda^0 \to p \pi^-.$ The correction factors depend on the momentum and polar angle of the tracks. Finally, a photon efficiency correction is applied to the ECL clusters in the ROE using a random removal algorithm, since photon reconstruction efficiency in data is always slightly smaller than photon reconstruction efficiency in simulation. A photon in MC is excluded from the reconstruction with a probability $1 - \omega$, where ω is the ratio of photon reconstruction efficiency in data and in simulation. To do so, we generate a repeatable random sequence of values between zero and one, and a given photon is removed if the corresponding random value is greater than ω . The ω ratios, which vary between 0.8 and 1.0, are extracted from data and simulation samples of $e^+e^- \rightarrow \mu^+\mu^- \gamma$ events as a function of missing momentum and its angular direction (θ,ϕ) as shown in [38].

B. Clusters multiplicity calibration

After applying all the efficiency corrections, the shapes of the $E_{\rm FCL}^{\rm extra}$ distribution in data and in simulation are slightly different. The discrepancy is found to be related to an incorrect modeling of the multiplicity of extra neutral clusters (n_{yextra}). Figures 2(a) and 2(b) show n_{yextra} and $E_{\rm ECL}^{\rm extra}$ distributions. Figures 2(c) and 2(d) show, as an $E_{\rm FCL}^{\rm extra}$ distributions for $n_{\gamma \text{extra}} = 3$ and example, $n_{\text{yextra}} = 5$, with the number of events in simulation scaled to data, in order to test that $E_{\mathrm{ECL}}^{\mathrm{extra}}$ shapes agree at fixed multiplicity n_{yextra} . The agreement is good at any fixed n_{yextra} (see Appendix A for the complete set of plots). Therefore, we conclude that simulation approximately models the $E_{\mathrm{ECL}}^{\mathrm{extra}}$ distribution in each multiplicity bin, while the expected normalization differs with respect to data by a few percent up to 20%. In order to correct the simulation expectation to match the data, we determine a bin-by-bin correction of $n_{\gamma \text{extra}}$ from three control samples. The first sample, referred to as the extra-tracks sample, is obtained by requiring two or more tracks in the ROE coming from the IP and with momenta less than 0.5 GeV. The corrections to n_{yextra} from the extra-tracks sample are used to reweight the $B\bar{B}$ background simulation. For the second sample, we reconstruct a $B^+ \to \bar{D}^{*0} \, \ell^+ \, \nu_\ell$ decay recoiling against the hadronic B_{tag} , and the resulting corrections are used to reweight the signal simulation for leptonic modes. The third sample is obtained by reconstructing two nonoverlapping hadronic tag B mesons with opposite charges in the event (double tag); this sample is used to reweight the signal simulation for hadronic modes. Typical correction factors vary between 0.8 and 1.2. Each control sample is discussed in detail in Appendix A.

This correction significantly improves the agreement between data and simulation. The residual systematic discrepancy in the $E_{\rm ECL}^{\rm extra}$ distribution is due to the limited sizes of the control and simulation samples used to derive

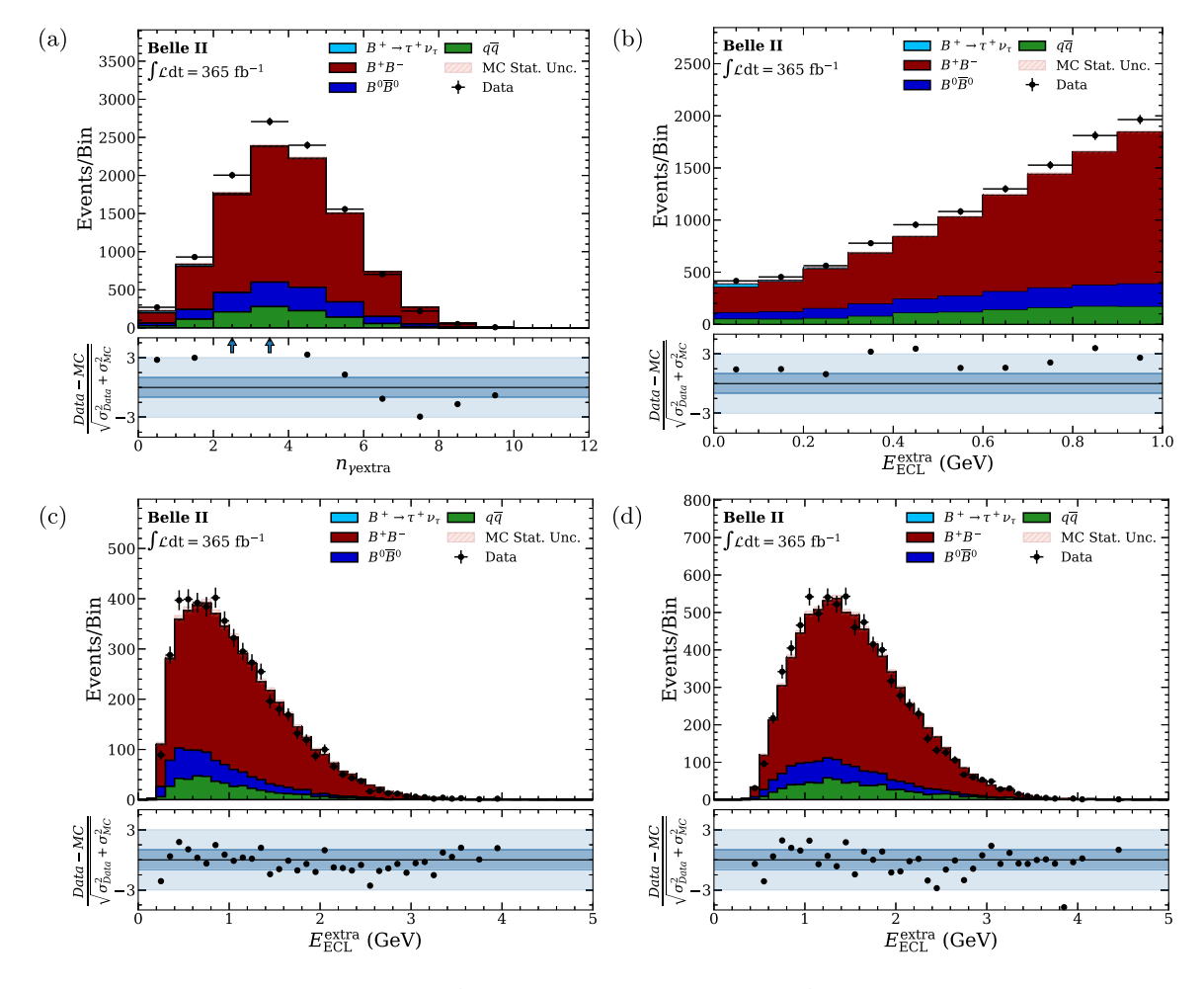


FIG. 2. First row: distributions of $n_{\gamma \rm extra}$ (a) and $E_{\rm ECL}^{\rm extra}$ (b) in data and simulation for $E_{\rm ECL}^{\rm extra} < 1$ GeV. Second row: distributions of $E_{\rm ECL}^{\rm extra}$ with $n_{\gamma \rm extra} = 3$ (c) and $n_{\gamma \rm extra} = 5$ (d). The number of events in simulation is scaled to the data for (c) and (d) to compare the shapes. The $B^+ \to \tau^+ \nu_\tau$ signal events are a small component of the full sample.

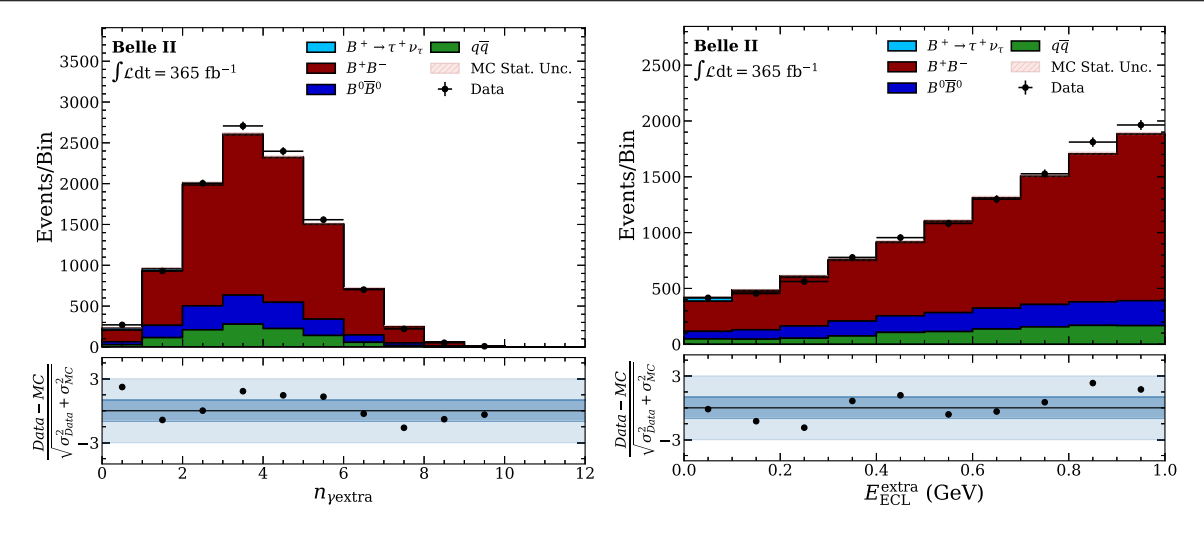


FIG. 3. Distributions of n_{yextra} (left) and E_{ECL}^{extra} (right) in data and simulation for $E_{ECL}^{extra} < 1$ GeV after applying the n_{yextra} calibration.

the correction. We describe the evaluation of the associated systematic uncertainty in Sec. VII.

We validate the procedure by comparing the reweighted MC distributions with data in the following sidebands: $E_{\rm ECL}^{\rm extra}$ sideband, requiring $E_{\rm ECL}^{\rm extra} > 500$ MeV; $M_{\rm bc}$ sideband, requiring $M_{\rm bc} < 5.26$ GeV/ c^2 ; $M_{\rm miss}^2$ sideband (leptons only), requiring $M_{\rm miss}^2 < 4$ GeV²/ c^4 ; $p_{\rm cand}$ sideband (hadrons only), requiring $p_{\rm cand} < 1.2$ GeV/c. In all cases, we find good agreement between MC simulation and data. Figure 3 shows $n_{\rm yextra}$ and $E_{\rm ECL}^{\rm extra}$ distributions after applying the corrections.

V. SIGNAL EXTRACTION

We use the $E_{\rm ECL}^{\rm extra}$ and $M_{\rm miss}^2$ variables to discriminate between signal and background: signal events are characterized by low $E_{\rm ECL}^{\rm extra}$ and large $M_{\rm miss}^2$. The signal contains two or three neutrinos for the hadronic and leptonic final states, respectively. These neutrinos produce a significant $M_{\rm miss}^2$ that follows a broader distribution than background processes. The additional neutrino in the leptonic final states leads to a larger value of $M_{\rm miss}^2$ on average compared to the hadronic modes. We exploit this behavior and the correlations by combining the $E_{\rm ECL}^{\rm extra}$ and $M_{\rm miss}^2$ distributions in a single two-dimensional binned probability density function (PDF).

We extract the branching fraction $\mathcal{B}(B^+ \to \tau^+ \nu_\tau)$ from a simultaneous binned maximum likelihood fit to all the four τ^+ categories. The PDFs are two-dimensional (2D) histograms of $M_{\rm miss}^2$ and $E_{\rm ECL}^{\rm extra}$ with 10×10 uniform binning, with $-10 < M_{\rm miss}^2 < 26~{\rm GeV^2/c^4}$ and $0 \le E_{\rm ECL}^{\rm extra} < 1~{\rm GeV}$. Figure 4 shows the 2D histogram PDFs of $E_{\rm ECL}^{\rm extra}$ and $M_{\rm miss}^2$ for signal and background in the $\tau^+ \to e^+ \ \nu_e \ \bar{\nu}_\tau$ channel (left plots) (similar for the $\tau^+ \to \mu^+ \ \nu_\mu \ \bar{\nu}_\tau$ channel) and in the

 $\tau^+ \to \pi^+ \ \bar{\nu}_\tau$ (right plots) (similar for the $\tau^+ \to \rho^+ \ \bar{\nu}_\tau$ channel).

We float five parameters in the fit: the common branching fraction $\mathcal{B}(B^+ \to \tau^+ \nu_\tau)$ and the total background yield for each of the four decay modes $n_{b,k}$, with $k=e^+,\mu^+,\pi^+$, or ρ^+ . The signal yields $n_{s,k}$ are not free parameters but depend on the common floating fit parameter $\mathcal{B}(B^+ \to \tau^+ \nu_\tau)$ and fixed quantities as follows:

$$n_{s,k} = 2n_{B^+B^-} \times \epsilon_k \times \mathcal{B}(B^+ \to \tau^+\nu_{\tau}) \tag{4}$$

with $n_{B^+B^-}=n_{\Upsilon(4S)}f^{+-}$, where $f^{+-}=0.5113^{+0.0073}_{-0.0108}$ is the branching fraction $\mathcal{B}(\Upsilon(4S)\to B^+B^-)$ estimated in [4]; ϵ_k is the efficiency to reconstruct in the category k a $B^+\to \tau^+\nu_\tau$ decay (for any kind of real τ decay). The efficiencies ϵ_k , estimated in simulation and corrected for MC simulated data mismodeling, are shown in Table III. Table III shows the composition of each reconstructed τ^+ decay in terms of decay mode. The table shows the relevant sizes of the cross feed contributions. The *other* component is mostly

TABLE III. Composition of each reconstructed τ^+ decay from $B^+ \to \tau^+ \nu_{\tau}$ in terms of decay mode. The row denotes the reconstructed final state, and the columns represent the generated decay mode. The off-diagonal entries reflect the amount of cross feed between channels.

Reco					
True	e ⁺ (%)	μ+ (%)	π ⁺ (%)	ρ+ (%)	Other (%)
$\overline{e^+}$	97	0.1	0.1	0	2.8
μ^+	0	87	0.9	0.1	12
π^+	0.1	3.3	55.7	16	24.9
ρ^+	0.4	4.5	27.8	61.2	6.1

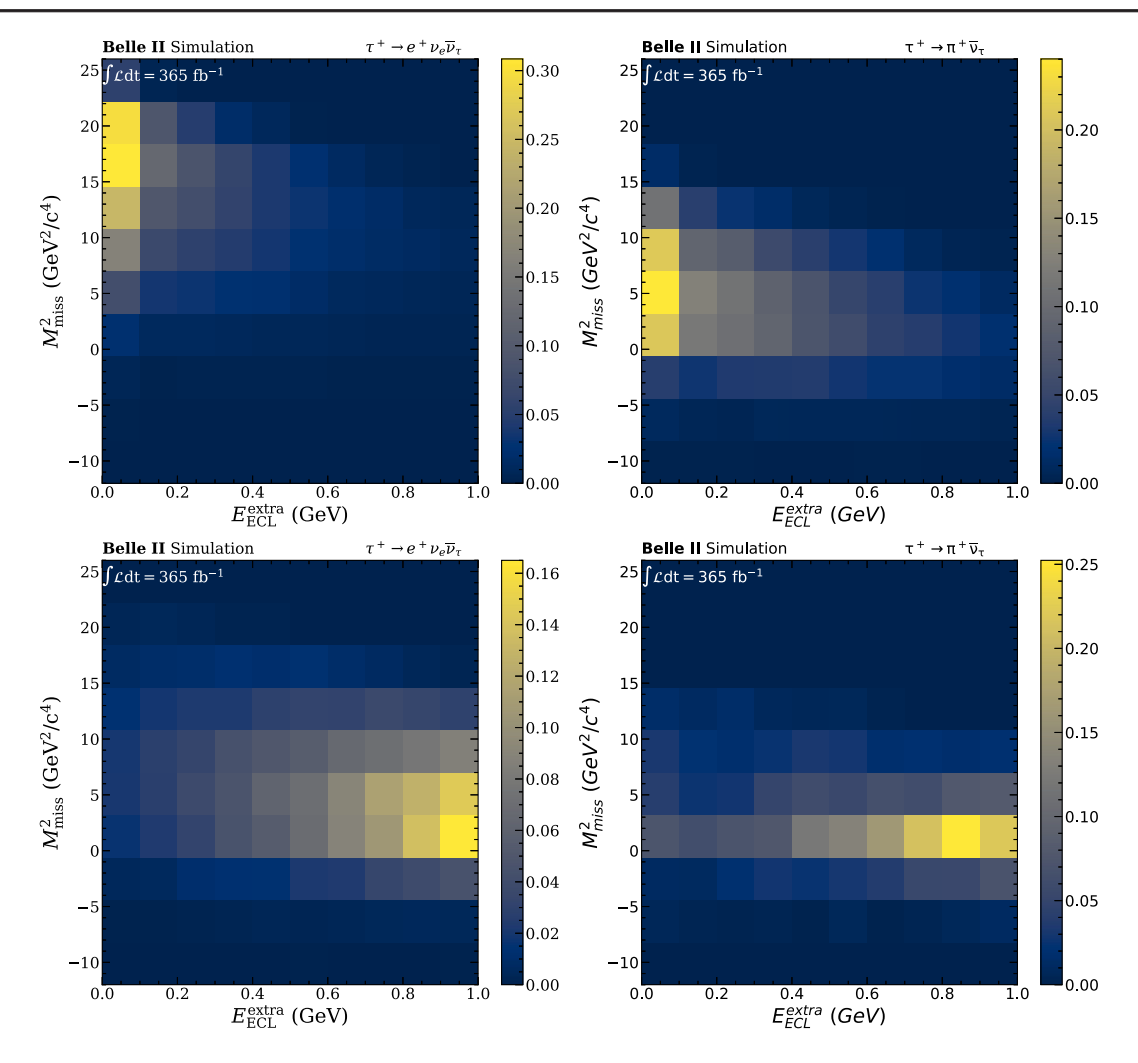


FIG. 4. Two-dimensional PDFs of $E_{\rm ECL}^{\rm extra}$ and $M_{\rm miss}^2$ from simulation for signal (top) and background (bottom) in the $\tau^+ \to e^+ \ \nu_e \ \bar{\nu}_\tau$ channel (left) (similar for the $\tau^+ \to \mu^+ \ \nu_\mu \ \bar{\nu}_\tau$ channel) and in the $\tau^+ \to \pi^+ \ \bar{\nu}_\tau$ (right) (similar for the $\tau^+ \to \rho^+ \ \bar{\nu}_\tau$ channel). The color represents the PDF probability in each bin.

multipion modes like $\tau^+ \to \pi^+ \pi^0 \pi^0 \bar{\nu}_{\tau}$ and $\tau^+ \to \pi^+ \pi^+ \pi^+ \pi^- \bar{\nu}_{\tau}$, where the additional pions are not reconstructed. Since in the fit we use templates from simulation that also include those modes and relative branching fractions this is completely taken into account in the final result.

VI. FIT RESULT

Performing the fit to the data we obtain

$$\mathcal{B}(B^+ \to \tau^+ \nu_{\tau}) = (1.24 \pm 0.41) \times 10^{-4},$$
 (5)

where the uncertainty is statistical only (stat.).

In order to check the goodness of fit, we generate pseudodatasets from the simulated distributions and repeat the fit on the obtained pseudodata. We observe that the χ^2 values obtained in pseudodata are worse than the χ^2 obtained in data for 11% of the cases. The χ^2 is defined as

$$\chi^2 = \sum_{i=1}^{100} \frac{(n_i - \theta_i)^2}{\sigma_{n_i}^2 + \sigma_{\theta_i}^2},\tag{6}$$

where the sum runs over the 100 bins of the distribution. Here, n_i represents the content of bin i in the pseudodata distribution, and θ_i is the corresponding value from the simulation. The terms σ_{n_i} and σ_{θ_i} denote the statistical uncertainties on the pseudodata and simulation, respectively.

In Fig. 5 we show the projections of the fit for $E_{\rm ECL}^{\rm extra}$ and $M_{\rm miss}^2$ distributions (in Appendix B we show the same projections for each τ^+ category). The comparison of fitted background yields with respect to MC simulation expectation is shown in Table IV. Table V shows $\mathcal{B}(B^+ \to \tau^+ \nu_\tau)$ obtained by fitting simultaneously the four τ^+ categories and fitting each category independently from each other.

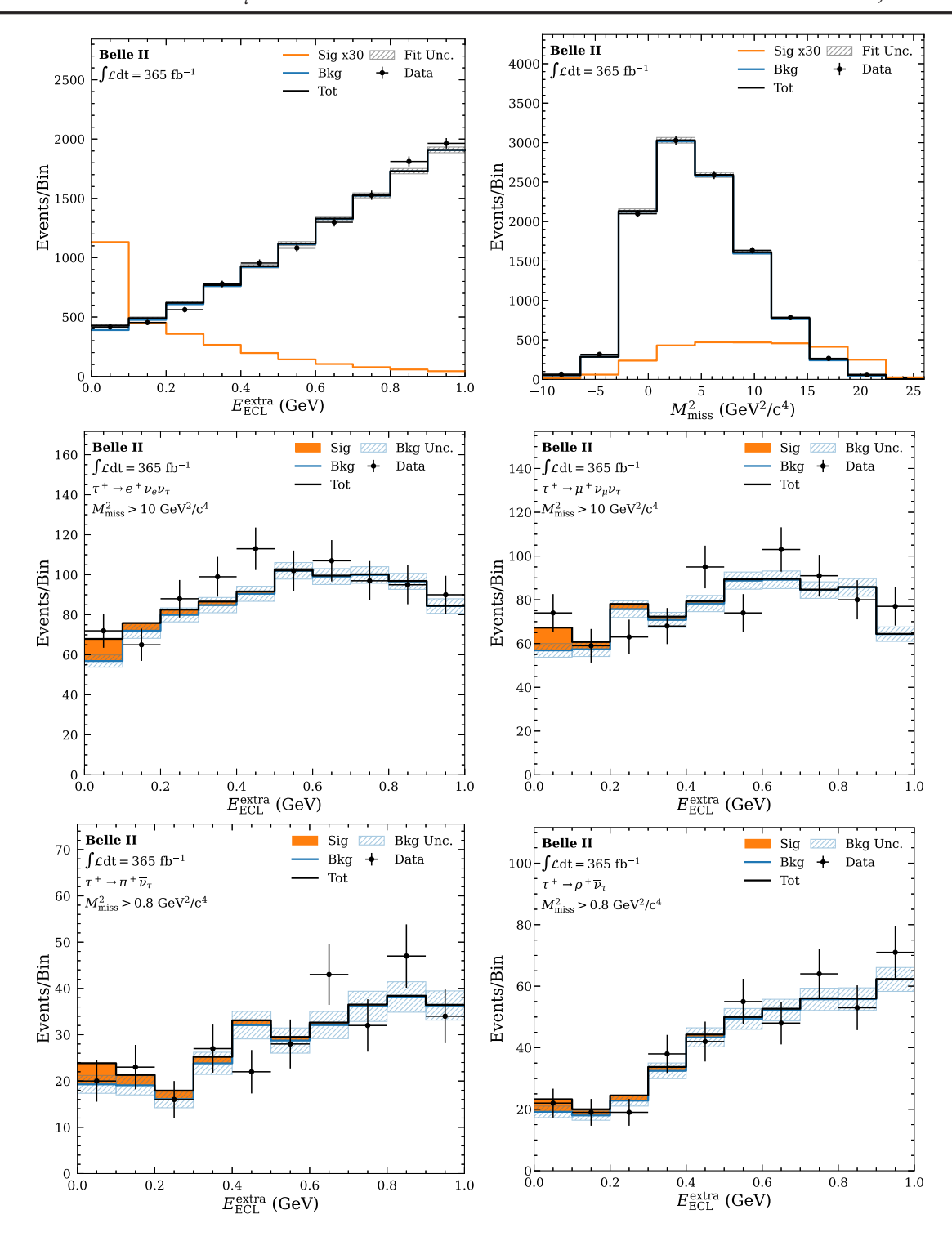


FIG. 5. First row: distributions of $E_{\rm ECL}^{\rm extra}$ (left) and $M_{\rm miss}^2$ (right) with the fit results superimposed. The signal MC simulated data are scaled by a factor of 30 to make it visible. Second row: distributions of $E_{\rm ECL}^{\rm extra}$ with the fit results superimposed for the leptonic channels in the signal enriched region $M_{\rm miss}^2 > 10~{\rm GeV^2/c^4}$. Third row: distributions of $E_{\rm ECL}^{\rm extra}$ with the fit results superimposed for the hadronic channels in the signal enriched region $M_{\rm miss}^2 > 0.8~{\rm GeV^2/c^4}$.

TABLE IV. Observed and expected values of the background yields in the fit. The expected values are estimated from a simulation corresponding to an integrated luminosity of 365 fb⁻¹.

Parameter	Observed value	Expected value
$\overline{n_{b,e^+}}$	4907 ± 71	4846 ± 24
n_{b,μ^+}	4620 ± 69	4493 ± 24
n_{b,π^+}	454 ± 22	461 ± 9
n_{b, ho^+}	772 ± 28	811 ± 11

TABLE V. Observed values of the signal yields and branching fractions, obtained from single fits for each τ^+ decay mode and the simultaneous fit.

Decay mode	n_s	$\mathcal{B}(10^{-4})$
Simultaneous	94 ± 31	1.24 ± 0.41
e^+ ν_e $\bar{\nu}_{ au}$	13 ± 16	0.51 ± 0.63
μ^+ ν_{μ} $\bar{\nu}_{ au}$	40 ± 20	1.67 ± 0.83
π^+ $ar{ u}_ au$	31 ± 13	2.28 ± 0.93
$ ho^+$ $ar u_ au$	6 ± 25	0.42 ± 1.82

VII. SYSTEMATIC UNCERTAINTIES

The main systematic uncertainties affecting the measurement are listed in Table VI. When uncertainties do not affect the signal yields, they are propagated directly to the branching fraction, as in the case of the number of $\Upsilon(4S)$, the fraction of B^+B^- pairs (symmetrizing the uncertainty to be $f^{+-}=0.5113\pm0.0108$ since it is not a dominant uncertainty), and the uncertainty on the tracking efficiency of the signal charged particle. Otherwise, the effect on the final result is estimated by varying the assumed quantity according to its uncertainty and propagating the effect to the PDF shapes, generating in this way a set of alternative PDFs. The fit is repeated with all the alternative templates, and the standard deviation of the fitted $\mathcal{B}(B^+ \to \tau^+ \nu_\tau)$ values is taken as the corresponding systematic uncertainty.

We evaluate the systematic uncertainty related to simulation statistics by fluctuating the bin contents of the 2D histogram PDFs 200 times, varying the bin content according to MC statistical uncertainties, and assuming a Poisson distribution. We obtain an uncertainty of 13.3%.

To evaluate the systematic corrections to the $n_{\gamma \rm extra}$ multiplicity we vary the bin-by-bin correction by applying 100 Gaussian variations, taking the variance from the corrections obtained from control studies. The resulting PDFs are used to repeat the fit. The standard deviation of the fit results is 5.5%, which is taken as a systematic uncertainty.

As a consistency check, we fit using distributions of $n_{\gamma \text{extra}}$ derived from data instead of those derived from simulated samples. We obtain a 2.4% relative difference with respect to the nominal result. This difference is negligible with respect to the largest systematic uncertainties, which arise from the simulated data sample size statistics and PDF corrections.

TABLE VI. Summary of systematic uncertainties (syst) on the fitted branching fraction presented as relative uncertainties. The effect of each source is evaluated in the simultaneous fit of the four signal modes. The last three sources do not affect the signal yields.

Source	Syst (%)
Simulation statistics	13.3
Fit variable PDF corrections	5.5
Decay branching fractions in the MC simulation	4.1
Tag B^- reconstruction efficiency	2.2
Continuum reweighting	1.9
π^0 reconstruction efficiency	0.9
Continuum normalization	0.7
Particle identification	0.6
Number of produced $\Upsilon(4S)$	1.5
Fraction of B^+B^- pairs	2.1
Tracking efficiency	0.2
Total	15.5

To account for possible discrepancies between data and simulation due to the branching fractions of the B and D decays used in the MC simulation, we apply 50 Gaussian variations to those branching fractions, with the variance set to the uncertainty of the latest PDG world average [2]. For poorly measured B decay modes present in the background simulation, we conservatively vary their branching fractions by 100%. Similarly, for poorly measured D decays, we group inclusive decay modes, e.g., $D \rightarrow K_L^0 X$, and vary their total branching fraction by 100%. The branching fractions of τ decays are known with high precision, and their uncertainties have a negligible impact. Repeating the fit with the modified MC samples, we obtain a 4.1% systematic uncertainty.

The $B_{\rm tag}$ reconstruction efficiency is calibrated with the $B^+ \to X \ell^+ \nu_\ell$ and $B^+ \to \bar D^{0(*)} \pi^+$ control samples. We generate 20 alternative sets of calibration factors from the covariance matrix of the nominal ones. Repeating the fit with the alternative corrections, we observe a 2.2% standard deviation in the fit results, which is taken as a systematic uncertainty.

The limited size of the off-resonance sample affects the reweighting of the continuum MC simulated data. Applying a bootstrapping procedure and resampling the training and test samples of the FBDT, we obtain 50 different sets of reweighting factors. Repeating the fit with this change we observe a standard deviation of 1.9% in the fit results, which is taken as a systematic uncertainty.

Events with a pion in the final state are assigned to the ρ (π) category if a π^0 is (is not) found to come from a $\rho^+ \to \pi^+\pi^0$ decay. Therefore, mismodeling of the π^0 reconstruction efficiency would affect only hadronic τ^+ decays. We study the data and MC simulation agreement for the π^0 efficiency using $D^{*0}(\to D^0\pi^0)\pi^+$ and $D^0 \to K^-\pi^+(\pi^0)$ decays for π^0 momenta in the range [0.05, 0.20]

and [0.20, 3.0] GeV/c, respectively, determining correction factors to the MC simulation for the π^0 efficiency. To obtain the systematic uncertainties, we follow a π^0 removal procedure. After generating a repeatable random sequence of values between zero and one, if the value is greater than the efficiency correction, the π^0 is removed, and the two γ 's are reassigned to the ROE; the event migrates from the $\tau^+ \to \rho^+ \bar{\nu}_\tau$ to the $\tau^+ \to \pi^+ \bar{\nu}_\tau$ category. We evaluate the systematic contribution by fitting the data on 50 different modified PDFs changing the random sequence. The difference between the average of the fitted branching fractions and the nominal fit result is negligible, while the standard deviation of the fitted branching fractions is 0.9%. Thus, we conclude that there is no bias in the result if the corrections are not applied and we set the systematic uncertainty to 0.9%.

We change the continuum fraction of the background by the statistical uncertainty of the off-resonance sample, producing 50 alternative background PDFs, obtained assuming a Poisson distribution. Repeating the fit with the different PDFs, we observe a standard deviation of fit results of 0.7%, which is taken as a systematic uncertainty.

The systematic uncertainty of the lepton and hadron identification efficiency and fake rates are extracted from pure samples of pions and leptons in $D^{*+} \rightarrow D^0 (\rightarrow K^- \pi^+) \pi^+$, $\Lambda^0 \rightarrow p \, \pi^-, \, K_S^0 \rightarrow \pi^+ \pi^-, \, J/\psi \rightarrow \ell^+ \ell^-$ data and MC sample. We evaluate the impact on the branching fraction fit by changing the shapes of the PDFs and the values of selection efficiencies according to 1σ variations of systematic uncertainty of lepton identification, π identification, and fake rates estimated in the control samples. We observe a standard deviation in the fit results of 0.6%.

We check the agreement of signal selection efficiency in data and MC simulation with a $B^+ \to \bar{D}^{*0} \ell^+ \nu_\ell$ control sample. After applying all the selections and calibrations, we find a data/MC simulation ratio equal to 0.96 ± 0.04 , which implies that no further efficiency correction is needed.

Moreover, we implement a signal embedding procedure on a sample of $B^+ \to K^+ J/\psi$ ($\to \ell^+ \ell^-$) ($\ell = e, \mu$), exploiting its clean experimental signature. In each event, $B^+ \to K^+ J/\psi$ is removed and replaced by a simulated $B^+ \to \tau^+ \nu_\tau$. This procedure is performed both on data and simulation, applying the standard $B^+ \to \tau^+ \nu_\tau$ reconstruction. The ratio of signal selection efficiencies estimated between data and MC simulation is 1.02 ± 0.18 , which confirms the agreement obtained from the $B^+ \to D^*$ $\ell^+ \nu_\ell$ control sample. The distributions of $E_{\rm ECL}^{\rm extra}$ and $M_{\rm miss}^2$ are also in good agreement between data and MC simulation for this embedding sample, as shown in Fig. 6.

We find evidence of signal with a significance of 3.0σ from a hypothesis test after convolving the likelihood profile with a Gaussian, whose width is set to the total systematic uncertainty. The test statistic is $-2\log(\mathcal{L}/\mathcal{L}_0)$, where \mathcal{L} (\mathcal{L}_0) is the value of the likelihood function when the signal yield is allowed to vary (is fixed to 0). We

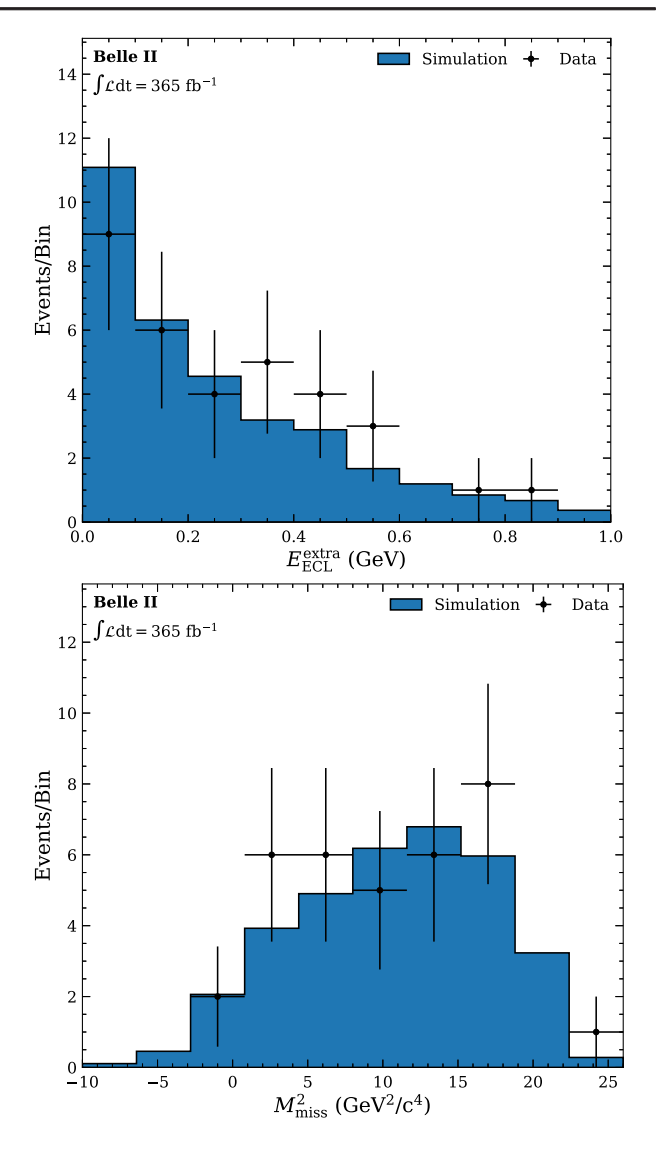


FIG. 6. Distributions of $E_{\text{ECL}}^{\text{extra}}$ (top) and M_{miss}^2 (bottom) for the signal embedding control sample.

generate 10⁶ pseudodatasets from the background-only PDF assuming no signal and repeat the fits. We obtain the significance from the p-value calculated as the fraction of fit results having a value of the test statistic smaller than the one observed in data.

VIII. CONCLUSIONS

We present a measurement of the branching fraction of the $B^+ \to \tau^+ \nu_\tau$ decay using 365 fb⁻¹ of electron-positron collision data recorded at the $\Upsilon(4S)$ resonance by the Belle II detector, using hadronic B tagging. For this measurement, we consider one-prong decays of the τ^+ lepton. We measure $\mathcal{B}(B^+ \to \tau^+ \nu_\tau)$ to be

$$\mathcal{B}(B^+ \to \tau^+ \nu_\tau) = [1.24 \pm 0.41(\text{stat}) \pm 0.19(\text{syst})] \times 10^{-4}$$
(7)

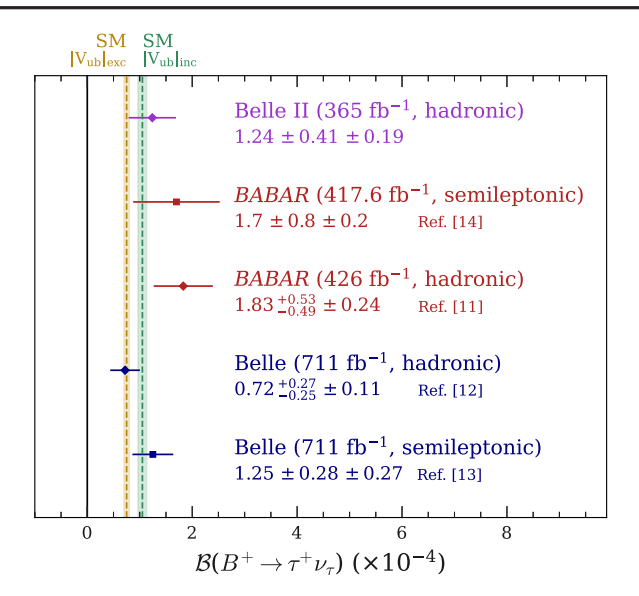


FIG. 7. Branching fraction $\mathcal{B}(B^+ \to \tau^+ \nu_\tau)$ measured by Belle II compared with the past measurements and the two SM expectation values, the yellow band calculated using the exclusive value $|V_{ub}| = (3.75 \pm 0.06 \pm 0.19) \times 10^{-3}$ and the green band with the inclusive value $|V_{ub}| = (4.06 \pm 0.12 \pm 0.11) \times 10^{-3}$.

with a significance of 3.0σ . The measured branching fraction is consistent with the current world average and with the SM prediction. Figure 7 shows a comparison of our $\mathcal{B}(B^+ \to \tau^+ \nu_\tau)$ measurement, with past measurements from *BABAR* and Belle, and SM predictions based on exclusive and inclusive determinations of $|V_{ub}|$ [4].

Assuming the SM and using $f_B = 190.0(13)$ MeV [3], we extract a measurement of the CKM matrix element

$$|V_{ub}|_{B^+ \to \tau^+ \nu_{\tau}} = [4.41^{+0.74}_{-0.89}] \times 10^{-3}.$$
 (8)

Even though we use a smaller data sample, the statistical uncertainty of this measurement is comparable to the previous hadronic tag analysis from BABAR (426 fb⁻¹) [11] and Belle (711 fb⁻¹) [12]. This improved sensitivity is due to the use of a new B tagging algorithm and an optimized selection.

ACKNOWLEDGMENTS

This work, based on data collected using the Belle II detector, which was built and commissioned prior to March 2019, was supported by Higher Education and Science Committee of the Republic of Armenia Grant No. 23LCG-1C011; Australian Research Council and Research Grants No. DP200101792, No. DP210101900, No. DP210102831, No. DE220100462, No. LE210100098, and No. LE230100085; Austrian Federal Ministry of Education, Science and Research, Austrian Science Fund (FWF) Grants DOI: 10.55776/P34529, DOI: 10.55776/J4731, DOI: 10.55776/J4625, DOI: 10.55776/M3153, and DOI: 10.55776/PAT1836324, and Horizon 2020 ERC

Starting Grant No. 947006 "InterLeptons"; Natural Sciences and Engineering Research Council of Canada, Digital Research Alliance of Canada, and Canada Foundation for Innovation; National Key R&D Program of China under Contract No. 2024YFA1610503, and No. 2024YFA1610504 National Natural Science Foundation of China and Research Grants No. 11575017. No. 11761141009, No. 11705209, No. 11975076, No. 12135005, No. 12150004, No. 12161141008, No. 12405099, No. 12475093, and No. 12175041, and Shandong Provincial Natural Science Foundation Project ZR2022JQ02; the Czech Science Foundation Grant No. 22-18469S, Regional funds of EU/MEYS: OPJAK FORTE CZ.02.01.01/00/22\ 008/0004632 and Charles University Grant Agency project No. 246122; European Research Council, Seventh Framework PIEF-GA-2013-622527, Horizon 2020 ERC-Advanced Grants No. 267104 and No. 884719, Horizon 2020 ERC-Consolidator Grant No. 819127, Horizon 2020 Marie Sklodowska-Curie Grant Agreement No. 700525 "NIOBE" and No. 101026516, and Horizon 2020 Marie Sklodowska-Curie RISE project JENNIFER2 Grant Agreement No. 822070 (European grants); L'Institut National de Physique Nucléaire et de Physique des Particules (IN2P3) du CNRS and L'Agence Nationale de la Recherche (ANR) under Grant No. ANR-23-CE31-0018 (France); BMFTR, DFG, HGF, MPG, and AvH Foundation (Germany); Department of Atomic Energy under **Project** Identification No. RTI 4002, Department of Science and Technology, and UPES SEED funding programs No. UPES/R&D-SEED-INFRA/17052023/01 and No. UPES/R&D-SOE/20062022/06 (India); Israel Science Foundation Grant No. 2476/17, U.S.-Israel Binational Science Foundation Grant No. 2016113, and Israel Ministry of Science Grant No. 3-16543; Istituto Nazionale di Fisica Nucleare and the Research Grants BELLE2, and the ICSC â Centro Nazionale di Ricerca in High Performance Computing, Big Data and Quantum Computing, funded by European Union NextGenerationEU; Japan Society for the Promotion of Science, Grant-in-Aid for Scientific Research Grants No. 16H03968, No. 16H03993, No. 16H06492, No. 16K05323, No. 17H01133, No. 17H05405, No. No. 18K03621, 18H03710, No. 18H05226, No. 19H00682, No. 20H05850, No. 20H05858, No. 22H00144, No. 22K14056, No. 22K21347, 23H05433, No. 26220706, and No. 26400255, the Ministry of Education, Culture, and Sports, Science, and Technology (MEXT) of Japan; National (NRF) Research Foundation of Korea No. 2021R1-F1A-1064008, No. 2022R1-A2C-1003993, No. 2022R1-A2C-1092335, No. RS-2016-NR017151, RS-2018-NR031074, No. RS-2021-NR060129, No. RS-2023-00208693, No. RS-2024-00354342 and No. RS-2025-02219521, Radiation Science Research Institute, Foreign Large-Size Research Facility Application Supporting project, the Global Science Experimental Data Hub Center, the Korea Institute of Science and Technology Information (K25L2M2C3) and KREONET/GLORIAD; Universiti Malaya RU grant, Akademi Sains Malaysia, and Ministry of Education Malaysia; Frontiers of Science Program Contracts No. FOINS-296, No. CB-221329, No. CB-236394, No. CB-254409, and No. CB-180023, and SEP-CINVESTAV Research Grant No. 237 (Mexico); the Polish Ministry of Science and Higher Education and the National Science Center; the Ministry of Science and Higher Education of the Russian Federation and the HSE University Basic Research Program, Moscow; University of Tabuk Research Grants No. S-0256-1438 and No. S-0280-1439 (Saudi Arabia), and Researchers Supporting Project number (RSPD2025R873), King Saud University, Riyadh, Saudi Arabia; Slovenian Research Agency and Research Grants No. J1-50010 and No. P1-0135; Ikerbasque, Basque Foundation for Science, State Agency for Research of the Spanish Ministry of Science and Innovation through Grant No. PID2022-136510NB-C33, Spain, Agencia Estatal de Investigacion, Spain Grant No. RYC2020-029875-I and Generalitat Valenciana, Spain Grant No. CIDEGENT/2018/020; The Knut and Wallenberg Foundation (Sweden), Contracts No. 2021.0174, No. 2021.0299, and No. 2023.0315; National Science and Technology Council, and Ministry of Education (Taiwan); Thailand Center of Excellence in Physics; TUBITAK ULAKBIM (Turkey); National Research Foundation of Ukraine, Project No. 2020.02/ 0257, and Ministry of Education and Science of Ukraine; the U.S. National Science Foundation and Research Grants No. PHY-1913789 and No. PHY-2111604, and the U.S. Department of Energy and Research Grant No. DE-AC06-76RLO1830, No. DE-SC0007983, No. DE-SC0009824, No. DE-SC0009973, No. DE-SC0010007, No. DE-SC0010073, No. DE-SC0010118, No. DE-SC0010504, No. DE-SC0011784, No. DE-SC0012704, No. DE-SC0019230, No. DE-SC0021274, No. DE-SC0021616, No. DE-SC0022350, No. DE-SC0023470; and the Vietnam Academy of Science and Technology (VAST) under Grants No. NVCC.05.02/25-25 and No. DL0000.05/ 26-27. These acknowledgements are not to be interpreted as an endorsement of any statement made by any of our institutes, funding agencies, governments, or their representatives. We thank the SuperKEKB team for delivering high-luminosity collisions; the KEK cryogenics group for the efficient operation of the detector solenoid magnet and IBBelle on site; the KEK Computer Research Center for on-site computing support; the NII for SINET6 network support; and the raw-data centers hosted by BNL, DESY, GridKa, IN2P3, INFN, and the University of Victoria.

DATA AVAILABILITY

The data that support the findings of this article are not publicly available upon publication because it is not technically feasible and/or the cost of preparing, depositing, and hosting the data would be prohibitive within the terms of this research project. The data are available from the authors upon reasonable request.

APPENDIX A: CALIBRATION OF n_{yextra}

The main source of the discrepancy in the $E_{\rm ECL}^{\rm extra}$ distribution between data and simulation is related to incorrect modeling of $n_{\rm yextra}$. Figure 8 shows the $E_{\rm ECL}^{\rm extra}$ shape for $n_{\rm yextra}=1,2,...9$, normalizing simulation to data. The $B^+ \to \tau^+ \nu_\tau$ signal affects only $n_{\rm yextra} \leq 2$. The simulation agrees well with the data for this variable. Therefore, we correct the normalization through bin-by-bin corrections of the $n_{\rm yextra}$ distribution using different control samples.

1. Extra-tracks control sample

We select a control sample of $B^+ \to \tau^+ \nu_{\tau}$ candidates that have more than two tracks in the ROE to evaluate the corrections to the $E_{\mathrm{ECL}}^{\mathrm{extra}}$ distribution for the $B\bar{B}$ background simulation. The control sample has the same $B\bar{B}$ background composition but no signal events. The control sample is defined using two different requirements on the charged tracks: IP tracks and signal-like tracks. The IP tracks criterion include all the tracks in the ROE with an impact parameter with respect to the IP less than 2 cm along the z axis, and 0.5 cm in the transverse plane, without any momentum requirement. The signal-like tracks criterion has the same definition but also requires a momentum greater than 0.5 GeV. We then require $N_{\text{IPTracks}} > 1$ and $N_{\mbox{\tiny Signal-like\,Tracks}} = 0.$ The average number of $N_{\mbox{\tiny IP\,Tracks}}$ in each event for this control sample is 3.2. Figure 9 shows the $n_{\gamma \text{extra}}$ distribution for data and MC simulation in this control sample for each signal channel, from which we extract correction factors to reweight the $B\bar{B}$ MC simulation background.

2. $B^+ \to \bar{D}^{*0} \, \mathscr{C}^+ \, \nu_{\mathscr{L}}$ control sample

We use the $B^+ \to \bar{D}^{*0}$ ℓ^+ ν_ℓ ($\ell^+ = e^+$, μ^+) control sample to extract the correction to reweight signal MC data for leptonic τ^+ decay categories. As for the $B^+ \to \tau^+\nu_\tau$ case, $E_{\rm ECL}^{\rm extra}$ (calculated from ROE) is expected to peak at zero. We reconstruct a hadronic $B_{\rm tag}$ candidate in each event with the hadronic FEI algorithm and a signal $B_{\rm sig}$ decaying to \bar{D}^{*0} ℓ^+ ν_ℓ and no extra tracks in the ROE. The requirements on the hadronic $B_{\rm tag}$ are the same as in the main analysis. For the signal side, we reconstruct the \bar{D}^{*0} in its decays to \bar{D}^0 π^0 and \bar{D}^0 γ , with $D^0 \to K^ \pi^+$, K_0^c π^+ π^- ,

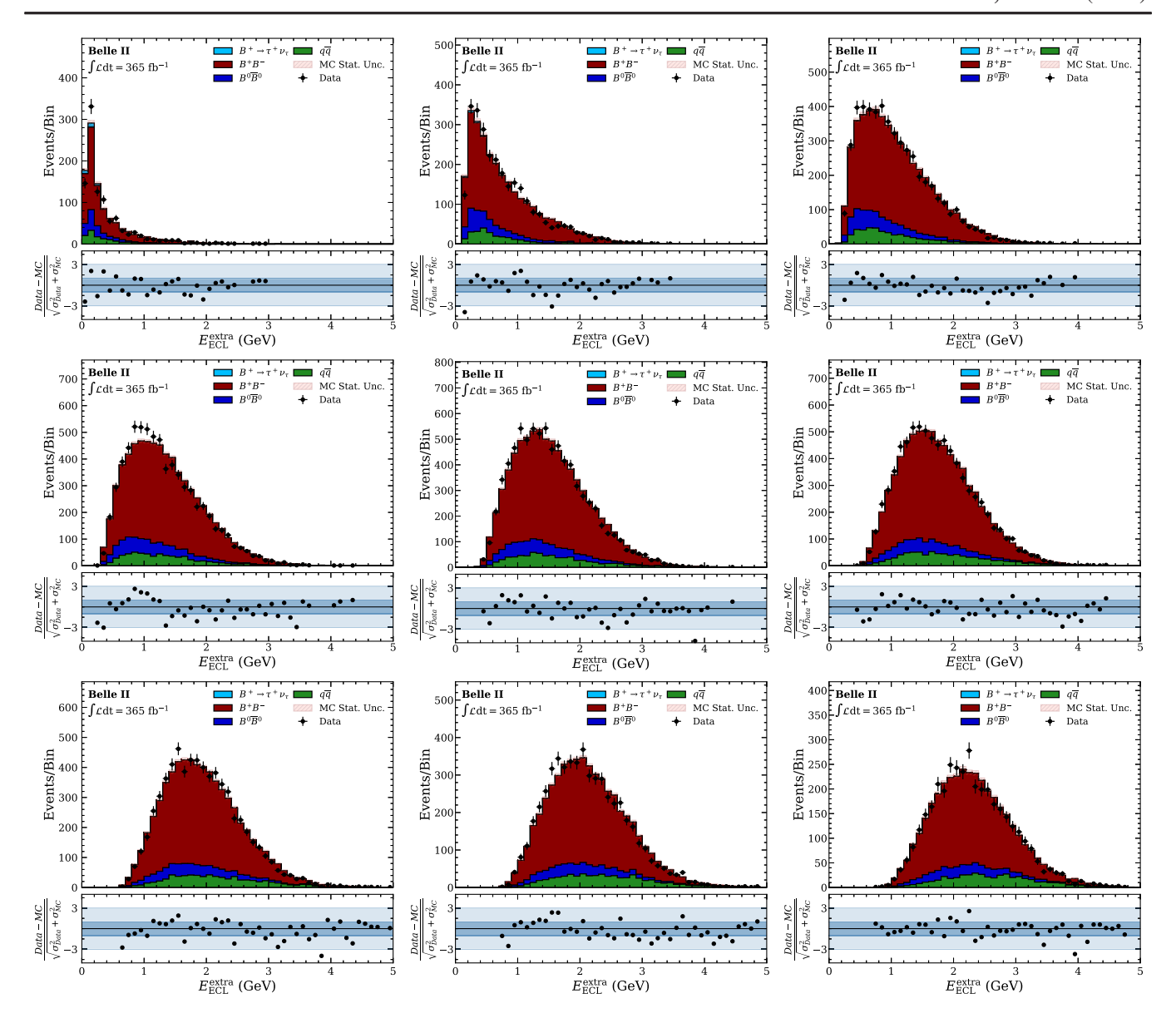


FIG. 8. Distribution of $E_{\rm ECL}^{\rm extra}$ as a function of $n_{\gamma \rm extra}$. Simulations are normalized to data. The first row shows $E_{\rm ECL}^{\rm extra}$ with $n_{\gamma \rm extra}=1,2,$ and 3. The second row shows $E_{\rm ECL}^{\rm extra}$ with $n_{\gamma \rm extra}=4,5,$ and 6. The third row shows $E_{\rm ECL}^{\rm extra}$ $n_{\gamma \rm extra}=7,8,$ and 9.

 $K^ \pi^+$ π^+ π^- . After the reconstruction, we apply all the corrections used in the main analysis to this sample. This includes continuum-reweighting and normalization, PID corrections, ROE clusters clean up, and corrections. To increase the purity of the sample, we require the momentum of the lepton to be greater than 1.5 GeV/c and the energy of the γ from the $\bar{D}^{*0} \to \bar{D}^0 \gamma$ decay to be greater than 170 MeV. The main component is correctly reconstructed $B^+ \to \bar{D}^{*0}$ ℓ^+ ν_ℓ , which is 84% of the full sample. The remaining 16% is composed of misreconstructed $B^+ \to \bar{D}^{**}$ ℓ^+ ν_ℓ , $B^+ \to \bar{D}^0$ ℓ^+ ν_ℓ , and other channels. Figure 10 (a) shows the $n_{\gamma \rm extra}$ distribution for data and MC data in this control sample, from which we extract correction factors to reweight MC signal simulation for leptonic τ^+ decay categories.

3. Double tag control sample

We use the double tag control sample to evaluate the corrections for the hadronic τ^+ decays in the signal simulation. We reconstruct events with two nonoverlapping B candidates with opposite charges with the hadronic FEI algorithm. We require no extra tracks in the ROE. The selection requirements for the hadronic $B_{\rm tag}$ are the same as the main analysis. The signal side is a second B reconstructed by the hadronic FEI. In the double tag control sample, $E_{\rm ECL}^{\rm extra}$ is expected to peak at 0 GeV as for $B^+ \to \tau^+ \nu_\tau$. We apply the same continuum reweighting and normalization, PID corrections, ROE clusters clean up, and corrections as for the main analysis. Figure 10(b) shows the data and MC data agreement in this control

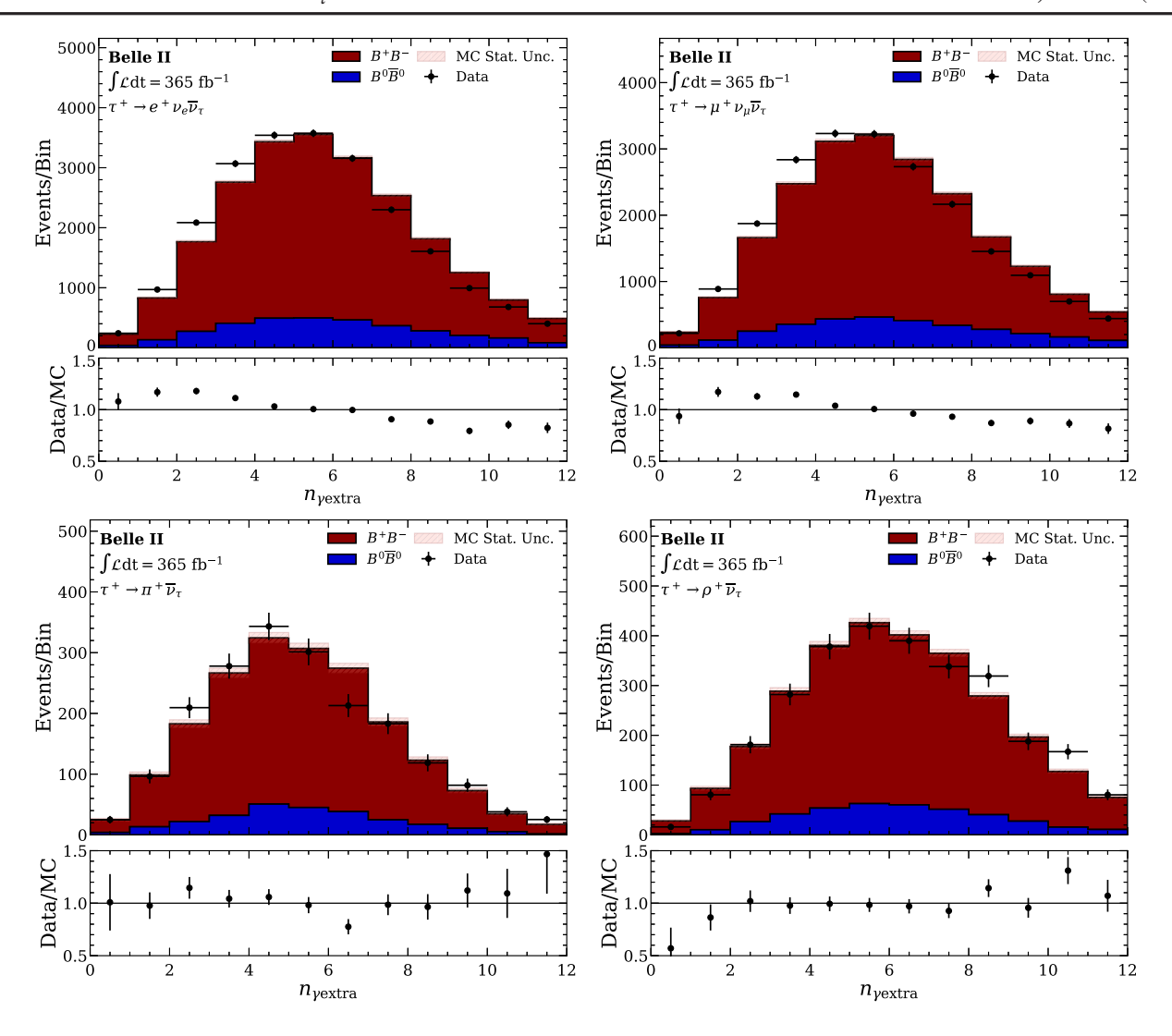


FIG. 9. Distributions of n_{yextra} in the extra-tracks control sample for the four signal channels. The bottom panel of each distribution shows the data/MC simulation ratio values and their uncertainties to be used as corrections for MC simulated data background for the analysis. The continuum component is subtracted since the correction factors are used only to correct the $B\bar{B}$ background component.

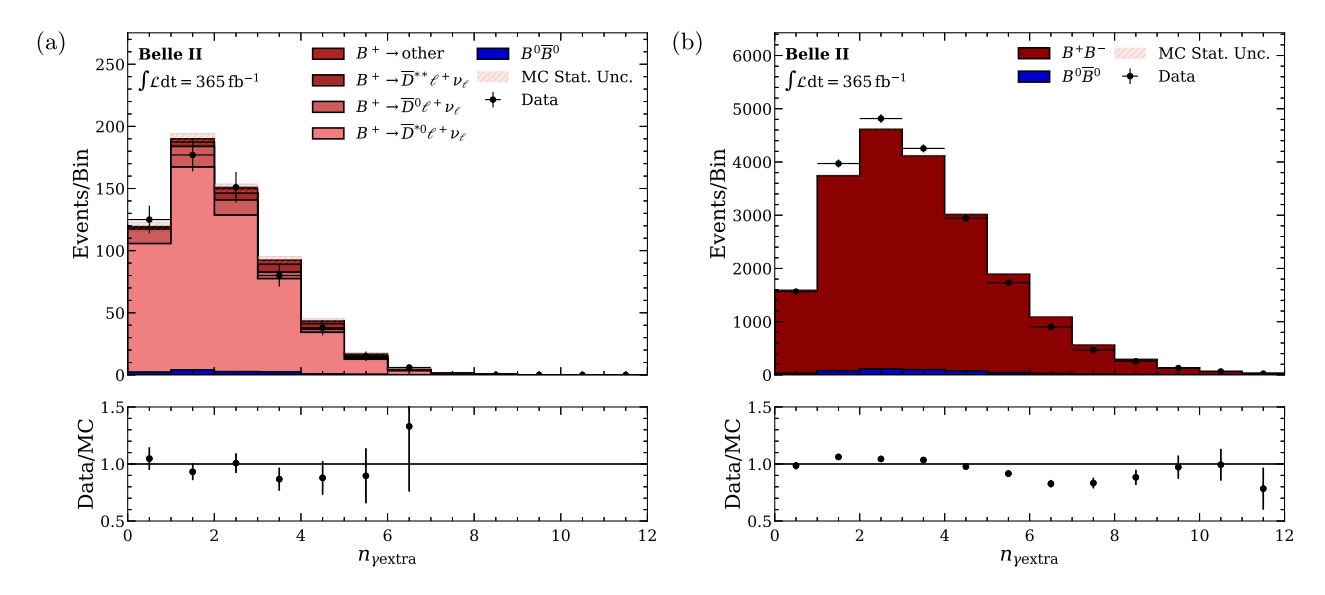


FIG. 10. Distributions of $n_{\gamma \text{extra}}$ in the $B^+ \to \bar{D}^{*0}$ $\ell^+ \nu_{\ell}$ (a) and double tag (b) control samples. The bottom panel of each distribution shows the data/MC simulation ratio values and their uncertainties to be used as corrections for leptonic and hadronic signal simulation, respectively. The continuum component is subtracted.

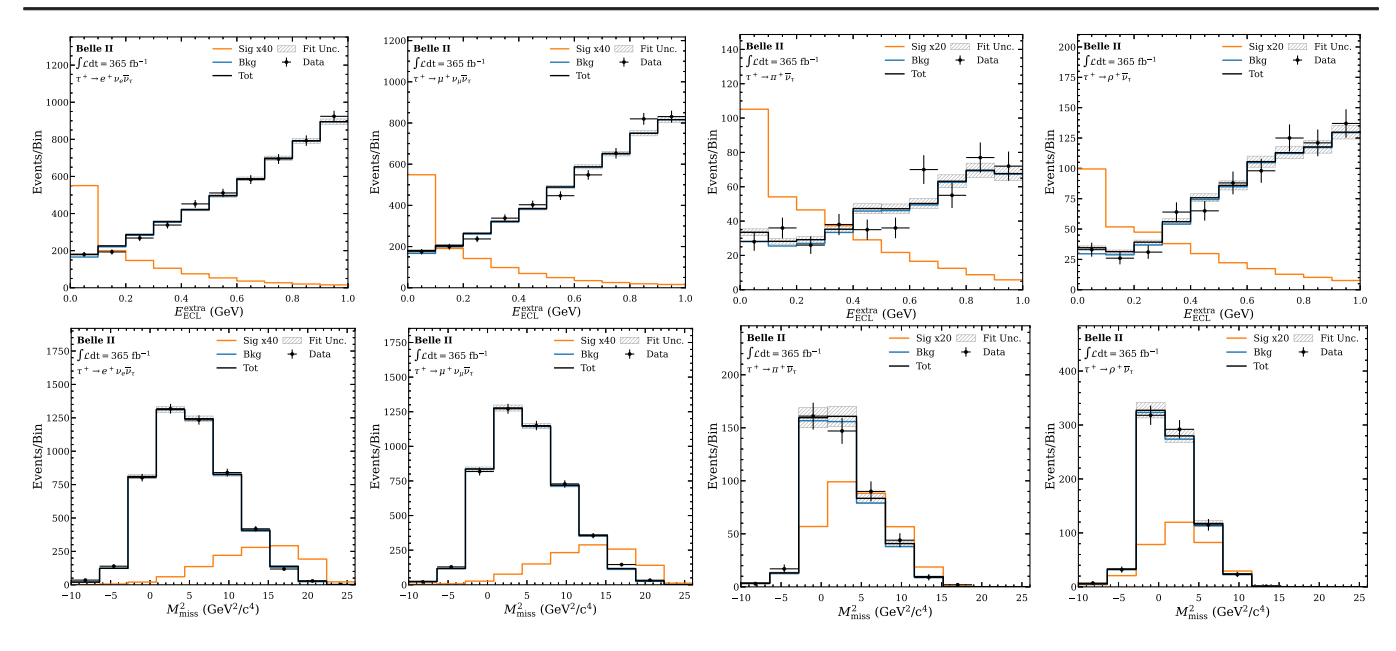


FIG. 11. Distributions of $E_{\text{ECL}}^{\text{extra}}$ (first row) and M_{miss}^2 (second row) with the fit results superimposed for each τ^+ category. The signal component is scaled by a factor of 40 for leptonic channels and 20 for hadronic channels in order to make it visible.

sample, from which we extract correction factors to reweight signal MC data for hadronic τ^+ decay categories.

APPENDIX B: DISTRIBUTIONS OF FIT VARIABLES

In Fig. 11 we show the projections of the fit for $E_{\rm ECL}^{\rm extra}$ and $M_{\rm miss}^2$ distributions for each au^+ category.

- [1] Throughout this paper, the inclusion of the charge-conjugate decay mode is implied unless otherwise stated.
- [2] S. Navas *et al.* (Particle Data Group), Review of particle physics, Phys. Rev. D **110**, 030001 (2024).
- [3] Y. Aoki et al., FLAG review 2024, arXiv:2411.04268.
- [4] S. Banerjee *et al.*, Averages of *b*-hadron, *c*-hadron, and τ-lepton properties as of 2023, arXiv:2411.18639.
- [5] W.-S. Hou, Enhanced charged Higgs boson effects in $B \to \tau \nu$, $\mu \nu$ and $\tau \nu X$, Phys. Rev. D **48**, 2342 (1993).
- [6] A. Crivellin, C. Greub, and A. Kokulu, Explaining $B \to D\tau\nu$, $B \to D^*\tau\nu$ and $B \to \tau\nu$ in a 2HDM of type III, Phys. Rev. D **86**, 054014 (2012).
- [7] J. Haller, A. Hoecker, R. Kogler, K. Mönig, T. Peiffer, and J. Stelzer, Update of the global electroweak fit and constraints on two-Higgs-doublet models, Eur. Phys. J. C 78, 675 (2018).
- [8] D. A. Bryman and R. Shrock, Improved constraints on sterile neutrinos in the MeV to GeV mass range, Phys. Rev. D 100, 053006 (2019).
- [9] A. W. M. Guerrera and S. Rigolin, ALP production in weak mesonic decays, Fortschr. Phys. 71, 2200192 (2023).
- [10] M. Jung, A. Pich, and P. Tuzón, Charged-Higgs phenomenology in the aligned two-Higgs-doublet model, J. High Energy Phys. 11 (2010) 003.

- [11] J. P. Lees *et al.* (*BABAR* Collaboration), Evidence of $B^+ \rightarrow \tau^+ \nu$ decays with hadronic B tags, Phys. Rev. D **88**, 031102 (2013).
- [12] K. Hara *et al.* (Belle Collaboration), Evidence for $B^- \rightarrow \tau^- \bar{\nu}_\tau$ with a hadronic tagging method using the full data sample of Belle, Phys. Rev. Lett. **110**, 131801 (2013).
- [13] B. Kronenbitter *et al.* (Belle Collaboration), Measurement of the branching fraction of $B^+ \to \tau^+ \nu_\tau$ decays with the semi-leptonic tagging method, Phys. Rev. D **92**, 051102 (2015).
- [14] B. Aubert *et al.* (*BABAR* Collaboration), Search for $B^+ \rightarrow \ell^+\nu_\ell$ recoiling against $B^- \rightarrow D^0\ell^-\bar{\nu}X$, Phys. Rev. D **81**, 051101 (2010).
- [15] I. Adachi *et al.* (Belle II Collaboration), Measurement of the integrated luminosity of data samples collected during 2019–2022 by the Belle II experiment, Chin. Phys. C 49, 013001 (2025).
- [16] T. Abe *et al.* (Belle II Collaboration), Belle II technical design report, arXiv:1011.0352.
- [17] K. Akai, K. Furukawa, and H. Koiso, SuperKEKB collider, Nucl. Instrum. Methods Phys. Res., Sect. A 907, 188 (2018).
- [18] K. Adamczyk *et al.* (Belle II and SVD Collaborations), The design, construction, operation and performance of the Belle II silicon vertex detector, J. Instrum. **17**, P11042 (2022).

- [19] D. Kotchetkov et al., Front-end electronic readout system for the Belle II imaging time-of-propagation detector, Nucl. Instrum. Methods Phys. Res., Sect. A 941, 162342 (2019).
- [20] D. J. Lange, The EvtGen particle decay simulation package, Nucl. Instrum. Methods Phys. Res., Sect. A 462, 152 (2001).
- [21] S. Jadach, B. F. L. Ward, and Z. Was, The precision Monte Carlo event generator KK for two-fermion final states in e^+e^- collisions, Comput. Phys. Commun. **130**, 260 (2000).
- [22] T. Sjöstrand, S. Ask, J. R. Christiansen, R. Corke, N. Desai, P. Ilten, S. Mrenna, S. Prestel, C. O. Rasmussen, and P. Z. Skands, An introduction to PYTHIA 8.2, Comput. Phys. Commun. 191, 159 (2015).
- [23] S. Jadach, J. H. Kuhn, and Z. Was, TAUOLA: A library of Monte Carlo programs to simulate decays of polarized tau leptons, Comput. Phys. Commun. 64, 275 (1990).
- [24] N. Davidson, T. Przedzinski, and Z. Was, PHOTOS interface in C++; Technical and physics documentation, Comput. Phys. Commun. 199, 86 (2016).
- [25] E. Barberio and Z. Was, PHOTOS: A universal Monte Carlo for QED radiative corrections. Version 2.0, Comput. Phys. Commun. 79, 291 (1994).
- [26] S. Agostinelli *et al.* (GEANT4 Collaboration), Geant4: A simulation toolkit, Nucl. Instrum. Methods Phys. Res., Sect. A 506, 250 (2003).
- [27] T. Kuhr, C. Pulvermacher, M. Ritter, T. Hauth, and N. Braun (Belle II Framework Software Group), The Belle II core software, Comput. Software Big Sci. 3, 1 (2019).
- [28] T. Keck *et al.*, The full event interpretation, Comput. Software Big Sci. **3**, 6 (2019).

- [29] F. Abudinén *et al.* (Belle II Collaboration), A calibration of the Belle II hadronic tag-side reconstruction algorithm with $B \to X \ell \nu$ decays, arXiv:2008.06096.
- [30] P. Cheema, Suppressing beam background and fake photons at Belle II using machine learning, EPJ Web Conf. 295, 09035 (2024).
- [31] S. Brandt, C. Peyrou, R. Sosnowski, and A. Wroblewski, The principal axis of jets. An attempt to analyze high-energy collisions as two-body processes, Phys. Lett. 12, 57 (1964).
- [32] E. Farhi, A QCD test for jets, Phys. Rev. Lett. 39, 1587 (1977).
- [33] G. C. Fox and S. Wolfram, Observables for the analysis of event shapes in e⁺e⁻ annihilation and other processes, Phys. Rev. Lett. 41, 1581 (1978).
- [34] T. Keck, FastBDT: A speed-optimized multivariate classification algorithm for the Belle II experiment, Comput. Software Big Sci. 1, 2 (2017).
- [35] Ed. A. J. Bevan, B. Golob, Th. Mannel, S. Prell, and B. D. Yabsley, The physics of the *B* factories, Eur. Phys. J. C **74**, 3026 (2014).
- [36] D. Martschei, M. Feindt, S. Honc, and J. Wagner-Kuhr, Advanced event reweighting using multivariate analysis, J. Phys. Conf. Ser. 368, 012028 (2012).
- [37] L. Feld, Continuum reweighting—Data-driven improvement of the continuum Monte Carlo simulation for Belle and Belle II, Master's thesis, Karlsruhe Institute of Technology (KIT), 2020.
- [38] H. Svidras *et al.*, Measurement of the data to MC ratio of photon reconstruction efficiency of the Belle II calorimeter using radiative muon pair events, Reports No. PUBDB-2021-05692, No. BELLE2-NOTE-PL-2021-008, BELLE, 2021.